Chapter 4

Co-seismic and post-seismic slip from multiple earthquakes in the northern Chile subduction zone: Joint study using InSAR, GPS, and seismology

Abstract

We use InSAR, GPS, and seismic data to constrain the location of co-seismic and post-seismic slip on the subduction interface in northern Chile. We invert body-wave seismic waveforms and InSAR data both jointly and separately. While the location of slip in the seismic-only, InSAR-only, and joint slip inversions is similar for the January 30, 1998, M_w 7.1 earthquake, there are some differences for the July 30, 1995, M_w 8.1 event, probably related to non-uniqueness of models that fit the seismic data. We use the joint inversion of the nearly point source 1998 earthquake to estimate station corrections at the seismic stations and relocate three $M_w > 7$ earthquakes from the 1980's. We demonstrate the sensitivity of the InSAR measurements by showing the probable detection of deformation from two M_w 6.6 events at 50 km depth. While we find that some previous centroid-moment-tensor (CMT) locations are systematically mislocated > 40 km toward the trench, our relocations are within error of previous global and local relocations. The 1995 earthquake did not rupture the entire seismogenic zone (as defined by previous earthquakes), and the 1998 and 1987 earthquake ruptured the bottom 10 km in depth. This variation in the depth of slip between small and large events is consistent with depth variations in material properties. InSAR and GPS data indicate that about 5% of the co-seismic moment from the 1995 earthquake was released during the 15 months immediately following the earthquake. This low magnitude of post-seismic deformation is anomalous compared to other recent subduction zone earthquakes, including the nearby 2001 Peru earthquake. In fact, because of atmospheric contamination, there is no unambiguous evidence for post-seismic deformation in the InSAR data between the 1995 and 1998 earthquakes, or after the 1998 earthquake.

4.1 Introduction

In a simple picture of the seismic cycle, stress within a given region increases in a simple monotonic fashion from tectonic motions. Once the stress surpasses a critical level it is released in a seismic event, and then begins to build up again. In reality, stress can be either increased or decreased in sudden jerks by earthquakes that occur nearby. Recent studies have advocated "stress triggering" – an earthquake on one part of a fault makes an earthquake on an adjacent part of the fault more (or less) likely to rupture (e.g., *Harris*, 1998; *Parsons et al.*, 2000). However, in some locations, determining the cause and effect relationship between earthquakes appears to be complex. For example, some models predict that the 1992 Landers, California earthquake should have made the 1999 Hector Mine, California, earthquake less likely to occur, but yet it still happened (*Harris and Simpson*, 2002). To advance our understanding of the seismic cycle, we require observations of earthquake interactions in a variety of environments, including subduction zones, where the largest earthquakes occur.

Five earthquakes with $M_w > 7$ have occurred in northern Chile since 1987 (Figure 4.1). In order to determine how these earthquakes might have interacted, we use both seismological and geodetic observations to determine which parts of the fault plane ruptured in each event. Eventually, the slip maps can be input into viscoelastic models and compared with observations of post-seismic deformation in order to constrain mantle rheology (e.g., *Thatcher et al.*, 1980), and possible triggering relationships. The distribution of co-seismic slip on the fault plane from each event can be compared to determine if there are areas that have had high slip in multiple earthquakes, *i.e.,* asperities (see, e.g., *Lay et al.*, 1982), or areas that had reduced slip in certain areas because of previous events. Locations on the fault plane that have slipped less than others provide information on earthquake hazard because they are more likely to slip in the future if they are not creeping aseismically (e.g., *Harris and Segall*, 1987).

Not all slip along the subduction zone interface occurs in earthquakes – stress can

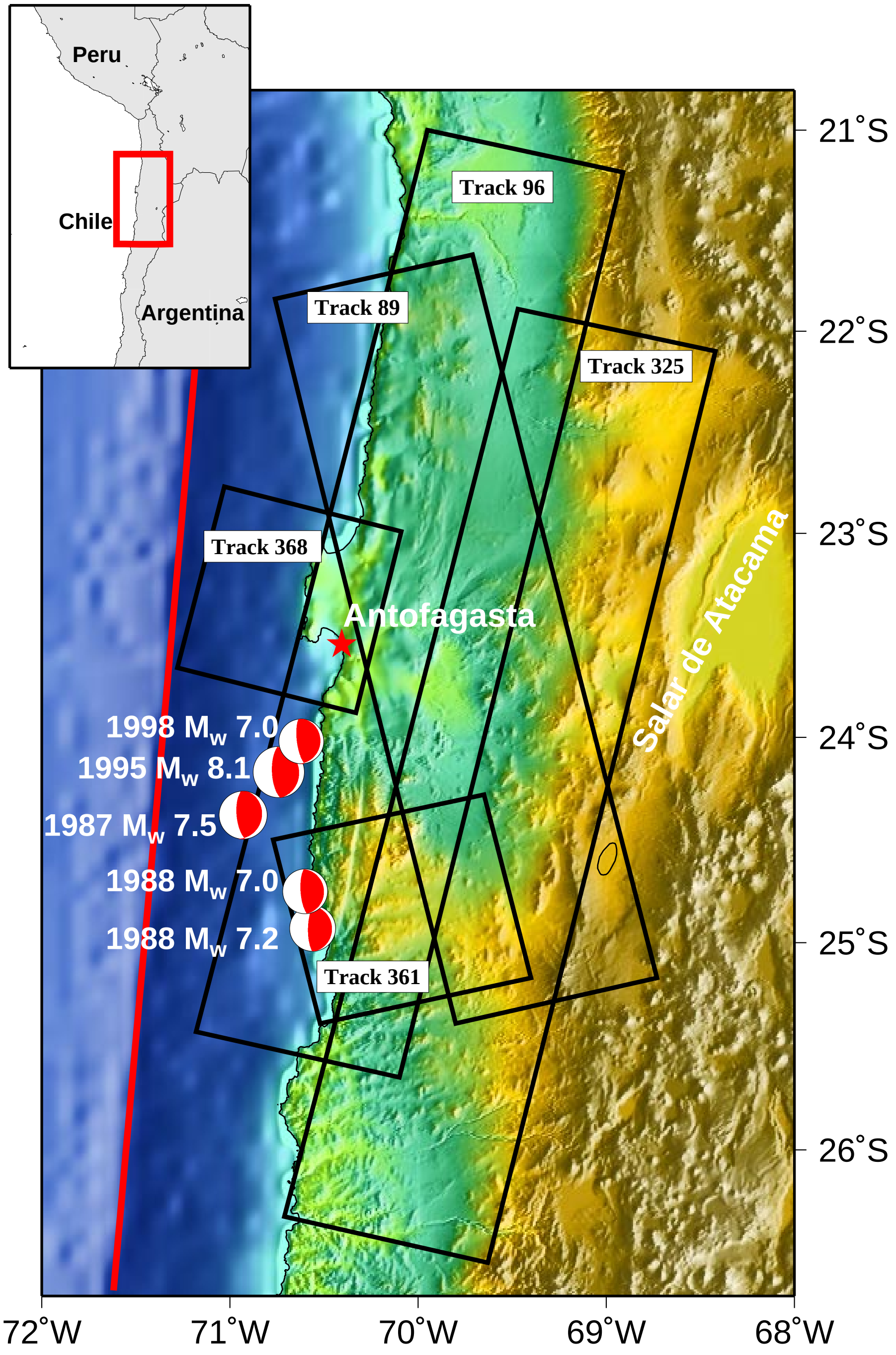

Figure 4.1: Locations of earthquakes with $M_w > 7$ between 1987-2000 in the northern Chile study area (see inset map). The star is the city of Antofagasta, and the mechanisms are the Harvard CMT locations. Squares show the outline of radar coverage used in this study.

be released in aseismic creep events (e.g., *Dragert et al.*, 2001; *Lowry et al.*, 2001b; *Miller et al.*, 2002; *Ozawa et al.*, 2002) or immediately following a large earthquake (post-seismic after-slip). We also use GPS and InSAR observations spanning 1995-1997 to constrain the magnitude and spatial-temporal distribution of post-seismic slip and compare it with the location of slip in the five $M_w > 7$ earthquakes.

4.2 Data used

Different datasets are available to study the five $M_w > 7$ earthquakes and the post-seismic deformation. Hereafter, we refer to the July 30, 1995 M_w 8.1 earthquake (discussed in Chapter 3) and the January 30, 1998 M_w 7.1 earthquake simply as the 1995 and 1998 earthquakes. We use a longer description for the other earthquakes: March 5, 1987, M_w 7.5; January, 19, 1988, M_w 7.0; February 5, 1988, (14:01 GMT) M_w 7.2. For the two most recent events (the 1995 and 1998 earthquakes), both geodetic data (primarily InSAR, see Figure 4.2, although GPS data is available for the 1995 event, see Chapter 3) and seismic waveforms are used. A re-analysis of the 1995 earthquake is warranted, because slip maps that used only seismic data, or seismic data and sparse geodesy (*Klotz et al.*, 1999; *Ihmlé and Ruegg*, 1997; *Ruegg et al.*, 1996) are not consistent with the InSAR observations (Chapter 3). A goal of this chapter is to determine a distribution of slip on the fault plane that explains all of the data for both the 1995 and the 1998 earthquakes. Using both datasets, we can well locate the 1998 earthquake, and determine the station corrections, *i.e.,* how the earth structure affects the travel times of the seismic waves radiated from this region. We use these station corrections and the P-wave travel time picks from the ISC to relocate the earthquakes in the 1980's, because no geodetic data is available. We use both InSAR and GPS data to study the post-seismic deformation over several different timescales. Within this region during the time period of interest, there were M_w 6.6 earthquakes in 1993 and 1996, but they are about 50 km deep. We study these earthquakes in order to test the sensitivity of InSAR and the GPS measurements, and the accuracy of the seismic locations.

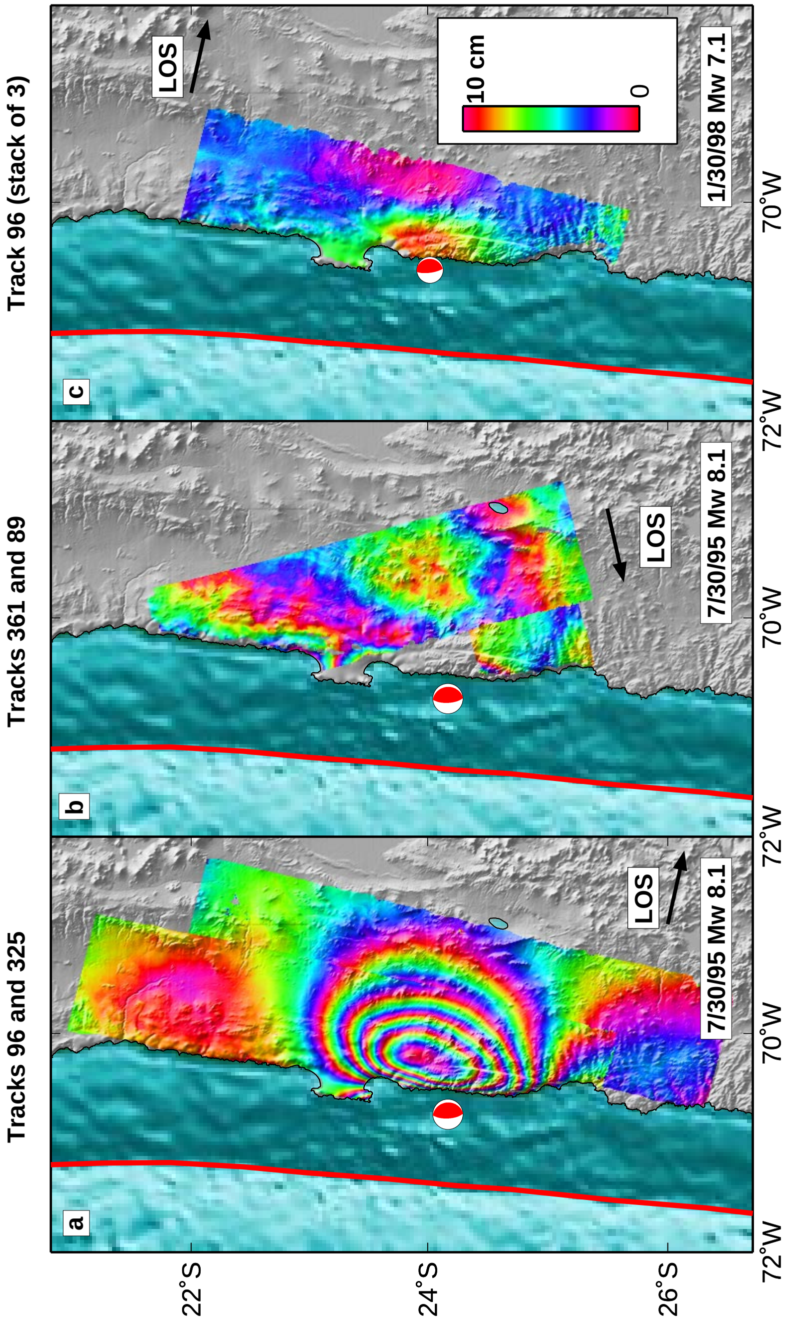

Figure 4.2: Contours of LOS displacement for the 1995 and 1998 earthquakes. The ground to satellite LOS direction is indicated by the arrows. a. Two of the three available tracks of descending data for the 1995 M_w 8.1 earthquake. Data from track 96 is from an interferogram spanning 10/9/1995-5/8/1992, and data from track 325 is from an interferogram spanning 9/19/1995-5/24/1992. b. The two ascending tracks of data for the same earthquake. Interferograms spanning 5/12/1993-9/26/1997 and 5/28/1993-10/12/1997 were used from tracks 361 and 89, respectively. c. One of the two tracks of descending data available for the 1998 M_w 7.1. This image is from a stack of three interferograms from track 96 spanning 5/31/1999-10/13/1997, 3/6/2000-4/21/1997, and 12/7/1998-4/21/1997.

The InSAR data that we use for this study is shown in Table 4.1. For the 1995 earthquake, we have used data from five orbital tracks (both ascending and descending) to make 12 interferograms, including an additional track and a few interferograms not used in Chapter 3. For the 1998 earthquake, we use a total of five interferograms from two orbital tracks with only descending orbits. We stack together multiple interferograms in an orbital track to reduce atmospheric effects (see Chapter 2). We sub-sample the interferograms to reduce the number of points from tens of thousands (Chapter 3) to hundreds or thousands (Chapter 2).

For the 1995 and 1998 earthquakes, we analyze the digital P and SH teleseismic displacement records from the global network. We only use seismographs that are at epicentral distances between 30° and 90°, because stations at smaller angles are effected by the mantle transition zone and at larger angles by core phases. We do not use all stations between 30° and 90°, but choose stations with a favorable azimuth distribution (Figure 4.3 and Figure 4.4), and remove stations that appear noisy or that have reversed polarity compared to adjacent stations which have the same polarity predicted by the focal mechanism. We visually inspected the displacement seismograms and removed a mean value or linear trend where necessary. We deconvolve the station response, remove frequencies higher than 1 Hz with a fourth-order two-pass butterworth filter (these frequencies are effectively damped out by attenuation, see below), and resample the data to a 0.2 second interval.

Like most previous studies, we use only vertical P and SH waves. At teleseismic stations, P waves are almost vertical, and because these waves are compressional, the vertical component is larger than the radial. In addition, the P-SV converted waves (vertically polarized S waves created as the P wave passes through local structure) are perpendicular to the P wave, and so are more prominent in the radial component. We use SH waves, because they are less sensitive to local structure than the P wave. Because of their direction of oscillation, SV waves are excited by vertical velocity variations, which are generally more important than the lateral variations that excite SH waves. We take the P wave data from the BH channel (20 samples/sec) and the SH data from the LH channel (1 samples/sec). The lower sample rate for the SH

Earthquake	Track	Frame(s)	Master image	Slave image	$B_\perp$ (m)
Pre-seismic	325	4059-4131	24 May. 1992	11 Jul. 1995*	120
1995 M_w 8.1	96	4041-4113	5 May 1992	9 Oct. 1995	50
	96	4041-4095	16 Apr. 1995	8 Oct. 1995	110
	96	4041-4095	16 Apr. 1995	30 Jul. 1995	200
	96	4041-4095	16 Apr. 1995	13 Oct. 1997	20
	325	4059-4131	24 May 1992	15 Aug. 1995	80
	325	4059-4131	24 May 1992	19 Sep. 1995	40
	325	4059-4131	11 Jul. 1995	19 Sep. 1995	130
	89	6741-6687	28 May 1993	12 Oct. 1997	150
	368	4077	14 Jul. 1995	18 Aug. 1995	50
	361	6687	12 May 1993	26 Sep. 1997	25
Post-seismic	96	4059-4113	21 Apr. 1997	31 Mar. 1996*	90
	96	4059-4113	30 Jul. 1995	12 Oct. 1997*	110
	96	4059-4113	30 Jul. 1995	13 Oct. 1997	220
	96	4059-4113	8 Oct. 1995	30 Jul. 1995	300
	96	4059-4113	31 Mar. 1996	30 Jul. 1995*	320
	96	4059-4113	1 Apr. 1996	21 Apr. 1997*	30
	96	4059-4113	2 Dec. 1996	31 Mar. 1996*	130
	96	4059-4113	21 Apr. 1997	2 Dec. 1996*	40
	96	4059-4113	21 Apr. 1997	12 Oct. 1997*	400
	96	4059-4113	17 Nov. 1997	31 Mar. 1996*	250
	96	4059-4113	17 Nov. 1997	1 Apr. 1996*	130
	96	4059-4113	17 Nov. 1997	2 Dec. 1996*	120
	96	4059-4113	17 Nov. 1997	21 Apr. 1997*	160
	96	4059-4113	13 Oct. 1997	8 Oct. 1995	80
	368	4077	24 May 1996	18 Aug. 1995	150
	368	4077	24 May 1996	22 Sep. 1995	330
	368	4077	25 May 1996	18 Aug. 1995	250
	368	4077	21 Dec. 1996	22 Sep. 1995	2
	368	4077	21 Dec. 1996	18 Aug. 1995	180
	325	4059-4131	19 Sep. 1995	15 Aug. 1995	30
	325	4059-4131	21 May 1996	19 Sep. 1995	10
	325	4059-4131	21 May 1996	15 Aug. 1995	30
	325	4059-4131	22 May 1996	19 Sep. 1995	80
	325	4059-4131	22 May 1996	15 Aug. 1995	110
1998 M_w 7.1	96	4059-4113	7 Dec. 1998	21 Apr. 1997	200
	96	4059-4113	6 Mar. 2000	21 Apr. 1997	110
	96	4059-4113	31 May 1999	13 Oct. 1997	90
	368	4077	10 Apr. 1999	19 Apr. 1996	50
	368	4077	26 Dec. 1998	21 Dec. 1996	50
Post-seismic	96	4059-4113	7 Dec. 1998	6 Mar. 2000	80

Table 4.1: ERS interferograms used to constrain co-seismic and post-seismic deformation from the 1995 M_w 8.1 and the 1998 M_w 7.1 earthquakes near Antofagasta, Chile. *Scenes used in the post-seismic stack (Figure 4.16).

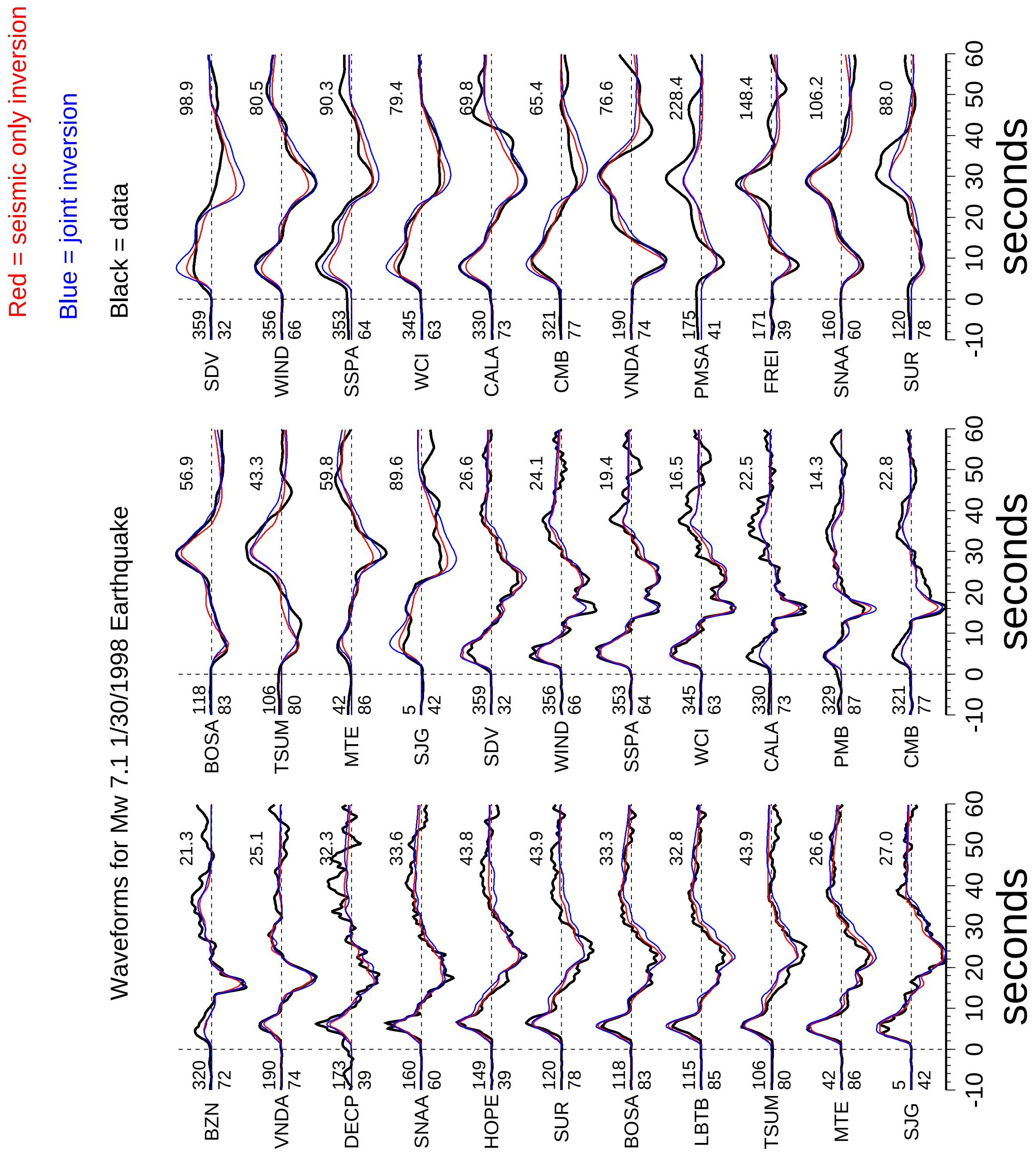

Figure 4.3: Seismic data (P and SH displacements as a function of time in seconds) used in the slip inversion for the 1998 M_w 7.1 earthquake (black lines) and calculated synthetics from the seismic-only (red lines) and joint inversions (blue lines). To the left of each trace is the station name, epicentral distance (lower number) and azimuth (upper number). The P wave records begin in the lower left with stations that are nearly due north and increase in azimuth clock-wise towards top of the page. The SH records begin when station SJG repeats and the azimuth begins near due north of the event. Each amplitude has been normalized by the maximum displacement, shown in microns to the upper right of each trace.

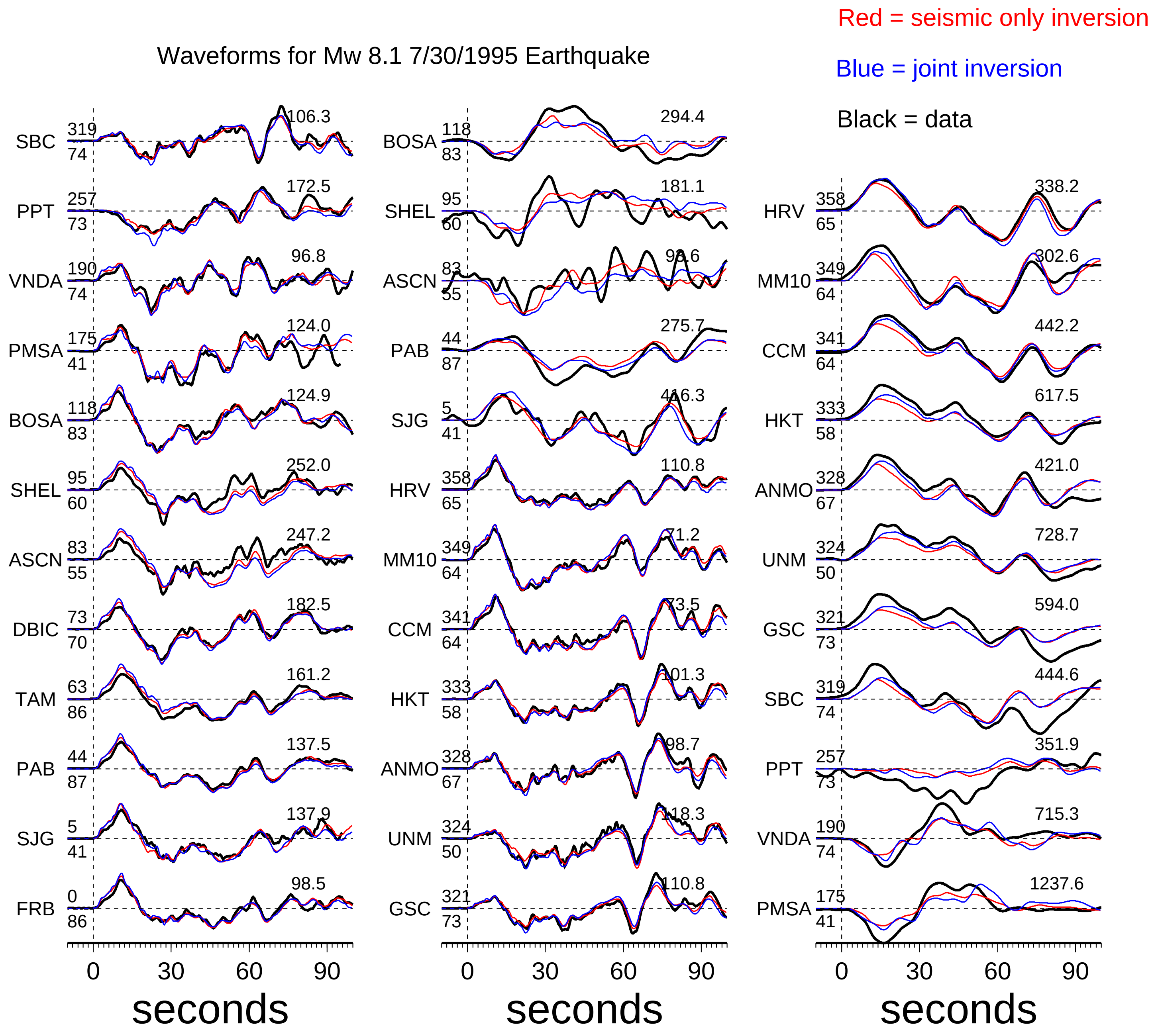

Figure 4.4: Seismic data (P and SH displacements as a function of time in seconds) used in the slip inversion for the 1995 M_w 8.1 earthquake (black lines) and calculated synthetics from the seismic-only (red lines) and joint inversions (blue lines). Conventions are the same as in Figure 4.3.

data is not a problem because of the longer period of the S waves, and the higher frequencies are removed by attenuation.

For the 1995 earthquake, we use seismic records that are 125 seconds long, although we cut the record shorter at a few stations to avoid the PP phase. We use 19 P and 16 SH records. It has been observed that this earthquake excited large amplitude, nearly monochromatic (14 seconds) oscillations on seismographs at all azimuths following the P wave, possibly caused by reverberations in the water column near the rupture area in the trench (*Ihmlé and Madariaga*, 1996). We ignore these oscillations as they do not become obvious in our data until after about 100 seconds, while the majority of moment release is in the first 70 seconds. Future work must examine the excitation mechanism of these waves to determine whether early time records are contaminated, and if additional information about the source process can be extracted from this monochromatic oscillation. For the 1998 earthquake we use 60 seconds of the seismogram following the first arrival of each wave, including 18 P and 15 SH stations.

4.3 Modeling strategy

Both geodetic and seismic data are non-unique – multiple slip distributions can explain either dataset. In Chapter 3, we discuss the difficulty of resolving fault slip parameters with a variety of geodetic data. Seismic data is different because the data are recorded as a time series. For dip-slip earthquakes, the waves radiated by slip on one patch are reflected (pP and sP are the most important) and can partially cancel the waves radiated on a different patch. For example, these radiated waves can cause a trade-off between the inferred depth of the fault slip and the source time function of the slip (e.g., *Christensen and Ruff*, 1985). Therefore, for most large subduction zone earthquakes, it is difficult to resolve slip as a function of depth using only teleseismic data (e.g., *Carlo et al.*, 1999). As we will show, as the earthquake rupture increases in time and complexity, more fault patches spanning a larger range of depths are involved, increasing the trade-offs and non-uniqueness of the seismic-only inversions.

Because the geodetic and seismic data are sensitive to different properties of the rupture, it is desirable to combine them together to reduce the range of acceptable models (e.g., *Wald and Graves*, 2001).

Several studies have combined seismic data with GPS (e.g., *Wald and Heaton*, 1994; *Ji et al.*, 2002b) and InSAR (e.g., *Hernandez et al.*, 1999; *Kaverina et al.*, 2002; *Delouis et al.*, 2002; *Salichon et al.*, 2003). We use the technique of *Ji et al.* (2002a) (hereafter called the Ji method) to invert for fault slip for the 1995 and 1998 earthquakes using both the seismic waveform and InSAR data. Details of the Ji method, including tests of the resolving power are given in *Ji et al.* (2002a), and here we only provide a brief summary. The seismic waveform is transformed into the wavelet domain so that both the temporal content (which contains information about the spatial location of slip) and frequency content (which constrains the duration of rupture on each patch, also called the rise time) of the waveform are used.

The location and dip of the fault plane for our joint inversions of the 1995 and 1998 earthquakes are about the same as that used in Chapter 3 (defined by the well located aftershocks of the 1995 earthquake). For the 1998 earthquake we use only a subsection of the fault plane, and assume the fault has a uniform dip (22°). For the larger 1995 earthquake, we model the fault interface as two subfaults with different dips (15° from 15-30 km depth and 25° from 30-60 km), which is slightly simpler than the curved fault used in Chapter 3 (see Figure 3.7). For the post-seismic slip inversions, the curved fault of Chapter 3 is used.

We compute the synthetic waveforms and static displacements by summing up nine point sources for each subfault (including directivity effects). The same wavelet transformation that is applied to the data is used for the synthetics. We use a 1-D layered velocity model with 14 layers (*Husen et al.*, 1999) and specify reasonable global values for the P and S quality factor (Q) for each layer to account for shallow attenuation. We convolve the attenuation function (t^*, e.g., *Lay and Wallace*, 1995) with the synthetics to account for attenuation of the seismic waveforms. This function reduces the amplitude of the waveform and removes periods shorter than t^*. We chose common values that are frequency independent (but see *Choy and Cormier*, 1986)–

1 second for P and longer for S (4 seconds) because most attenuation mechanisms involve shearing.

Because fitting the seismic waveform is non-linear, we use simulated annealing (*Rothman*, 1986) to explore parameter space and find the best fit model parameters. This iterative inversion algorithm is designed to avoid local minima by searching broadly through parameter space in initial steps, and then in later iterations to focus on regions that well fit the data (e.g., *Sen and Stoffa*, 1995). The difficult part of using this algorithm is deciding how to transition from the global to detailed search of parameter space (called the cooling schedule, e.g., *Basu and Frazer*, 1990). However, because the misfit functions has been normalized in the Ji method, the values chosen by *Ji et al.* (2002b) appear to work well for a variety of problems. We have performed a few tests along the lines suggested by *Basu and Frazer* (1990), and found that the parameters used by *Ji et al.* (2002b) seem robust for the earthquakes studied here.

For each subfault, we solve for the slip amplitude and direction, rise time and rupture velocity. The slip amplitude and direction are the same as the parameters studied in Chapter 3. The rise time indicates the length of time it takes for the fault patch to slip (prescribed as a modified cosine function, *Hartzell et al.*, 1996) and the rupture velocity specifies the speed of the local rupture front. Our inversion is not free to chose any value of these parameters – we chose extremal bounds for each parameter and a discretization interval. For both earthquakes we discretize the fault with uniform patches – 20 along strike by 10 in dip for the 1998 earthquake (5 by 5 km); and for the 1995 event 30 patches along strike and 14 in depth (10 by 10 km). We do not solve for quadratic ramps for the InSAR data as part of the inversion process as we did in Chapter 3 to correct for orbital errors and inter-seismic deformation. We calculate slip and ramps from a geodetic-only inversion, then remove the ramps from the InSAR data which is used in the inversion.

We define the best fit model as having the lowest objective function, given as: $E_{wf} + W_I * E_I + W_c * C$, where E_{wf} is the waveform misfit, E_I is the InSAR misfit, C are the constraints on the gross properties of the slip, and W_I and W_c are the relative weighting applied to the static misfit and the constraints. The L2 norm (or least squares) misfits are calculated for the seismic and InSAR data. For the seismic misfit, the P waves are weighted twice as much as the SH waves. The gross properties of the slip are constrained by minimizing the difference in slip between adjacent patches, and penalizing models with large moment, so that we find the smoothest slip distribution with the smallest moment that explains the data (e.g., *Hartzell and Heaton*, 1983; *Hartzell et al.*, 1996). There is some ambiguity to picking the appropriate weighting between datasets (e.g., *Kaverina et al.*, 2002), so we explore different values of W_I and W_c such that both datasets can be fit.

We use the IASPEI91 (1-D) travel time tables to calculate the first P arrival at each seismic station. Because of three-dimensional velocity variations and station timing errors, these predicted arrivals might be off by several seconds. We empirically correct the timing in two steps: (1) hand-picking arrival times at stations that are obviously wrong; (2) performing a preliminary inversion and shifting the seismograms to match the predicted waveforms.

4.4 Results

4.4.1 1998 earthquake

For both the 1998 and 1995 earthquakes, we have considered just the seismic data, just the InSAR data and both data sets together (see Figure 4.5). For all three inversions, the M_w 7.1 earthquake looks like a point source with most of the slip occurring near the hypocenter (as determined by the NEIC). The maximum slip was constrained to be less than 3 m, and is about 1 m for the seismic and InSAR inversions and about 2 m for the joint inversion. For this joint inversion, we use the weighting values $W_I = 1$ (the relative weighting of the geodetic to seismic data) and $W_c = 0.1$ (the relative weighting of the misfit to the constraints), the same as those used by *Ji et al.* (2002b). The seismic moments for the InSAR, seismic and joint inversions are: 5.2, 7.1 and 7.6 × 10^{19} Nm; or M_w 7.1, 7.2 and 7.2. We discuss reasons that the moment of the static and joint models might be larger below. The rise time was constrained to be between 2 and 10 seconds and had an average value of 3.8 seconds. The rupture velocity varied between 2.7 and 3.3 km/s, and had an average value of 3.1 km/s. The rake angle was allowed to vary between 70° and 140° (centered on the Harvard value of 105°, e.g., *Dziewonski et al.*, 1999), and the mean value for all inversions is about 103°. The Harvard mechanism for this event (like other small earthquakes discussed below) is located about 40 km west of the centroid of our model.

The synthetic waveforms from the seismic only and joint inversions are shown in Figure 4.3. The fit to the data is slightly degraded by adding the InSAR data, particularly at long periods. We are working to understand the misfit in the waveforms and the large moment of the static and joint inversions. There are at least four possible explanations: (1) The hypocenter depth could be slightly incorrect – we assume the NEIC location, but a location error or 10 km or more is possible; (2) we do not solve for orbital ramps (see Chapter 3); (3) we have not fully optimized the weighting of the datasets relative to each other or to the smoothness and moment minimization constraints; (4) the InSAR data is contaminated by atmospheric effects or inter-seismic/post-seismic deformation. Residual interferograms (subtracting predicted interferograms from the the InSAR only and joint models) are shown in Figure 4.6.

4.4.2 1995 earthquake

The spatial distributions of slip from the seismic only, InSAR only, and joint inversions are shown in Figure 4.7. This joint inversion only includes data from track 96, and we are currently working on inversions using all of the InSAR data. There are differences between the seismic only and InSAR only inversions, with the seismic model placing more slip near the hypocenter, while the InSAR slip distribution is centered on the Harvard CMT, as would be expected. Previous body wave only inversions for fault slip also place more slip near the hypocenter than inversions that include surface waves and/or geodetic data (see Chapter 3). The discrepancy between the location of slip in body wave only and other inversions might be related to the fact that slip was

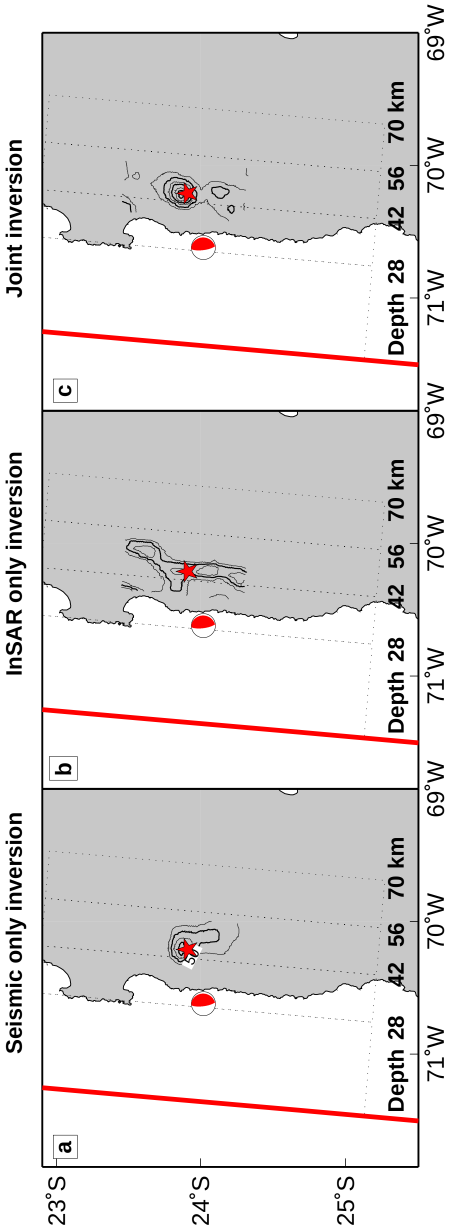

Figure 4.5: Contours of slip from the 1998 M_w 7.1 earthquake from inversions using only seismic data (a.), only InSAR data (b.), and both datasets (c.). The maximum slip is about 1 m and the contour interval is 0.2 m. The NEIC location is shown as the red star. The focal mechanism is from the Harvard catalog and is located about 40 km from the slip.

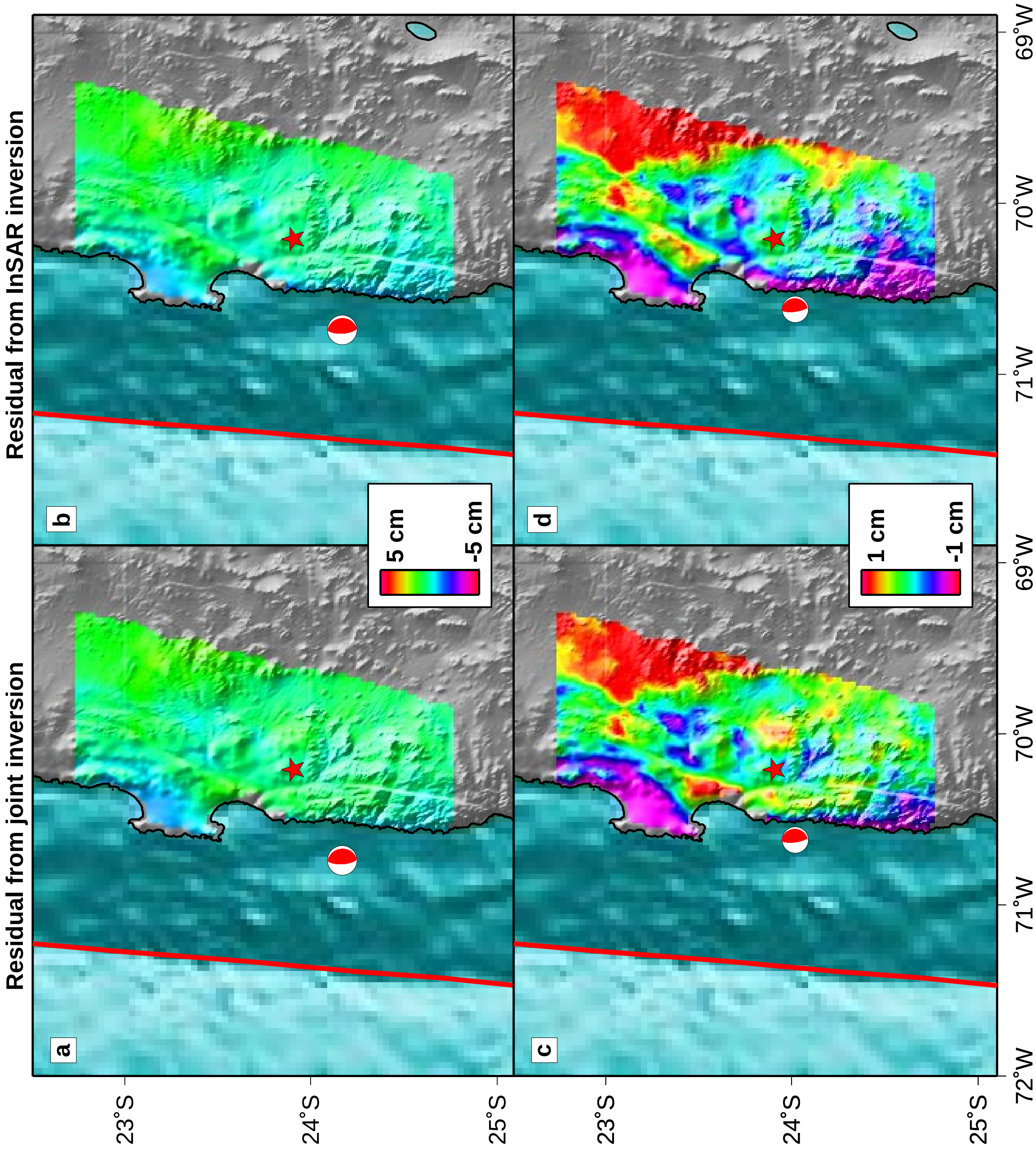

Figure 4.6: Residual of the InSAR data from track 96 for the 1998 M_w 7.1 from the inversions using only the InSAR data (a. and c., RMS 0.71 cm) and both seismic and InSAR data (b. and d., RMS 0.79 cm). a. and b. The residual at the original wrap rate used in Figure 4.2, while c. and d. show the same residuals at an expanded color interval.

very slow late in the rupture, or because of non-uniqueness in the body wave data. For this dip-slip event, there are complex trade-offs between slip and slip location because of the up and down polarity of waves reflected off the surface (*e.g.,* pP and sP), as mentioned above. The long rupture time of this event ($>$ 60 seconds) allows many possible slip distributions, while the much shorter rupture time of the 1998 earthquake seems to make the inversion less non-unique.

The maximum slip was constrained to be less than 7 m, and for the seismic, InSAR and joint inversions the maximum slip is: 4.4, 6, and 6.6 m. The seismic, InSAR and joint inversions have seismic moments of: 1.5×10^{21} Nm (M_w 8.0), 2.0×10^{21} Nm (M_w 8.1), and 2.2×10^{21} Nm (M_w 8.1). The weighting parameters are $W_I = 1$ and $W_c = 0.1$ for this joint inversion. The rake angle was allowed to vary between 70° and 140° (Harvard value of 87°), and the mean value (estimated only at patches with non-zero slip) for all inversions is about 108°. The rise time was constrained to be between 2 and 20 seconds and had an average value of between 7-9 seconds (for the seismic-only and joint inversions, respectively). The average rupture velocity of 3.0 km/s (constrained between 2.8-3.2 km/s) is within the range of previously determined values (2.5-3.2 km/s (*Delouis et al.*, 1997; *Ihmlé and Ruegg*, 1997; *Carlo et al.*, 1999). The moment and rake values fall within the range of values from previous inversions (Chapter 3).

Some details of the slip distribution are different between the joint inversion in Figure 4.7 and in Figure 3.10, because of differences in how fault slip is parameterized. For example, in Figure 3.10, there is a large amount of slip to the south-west of the CMT around 25°S, while there is little slip in the joint inversion. In Chapter 3, where we used only geodetic data, we varied the size of the fault patches to maximize resolution of the model parameters. Because only on-shore data was available, fault patches near the trench are large, and so slip on those patches is averaged over a large spatial area. For the joint inversion, we use small subfaults with a smoothing constraint (e.g., *Hartzell and Heaton*, 1983) allowing for greater localization of the slip. Neither the seismic or InSAR data well resolves slip near the trench (tsunami waveforms or water-column reverberations must be used, e.g., *Ihmlé and Madariaga*, 1996), but the addition of the seismic data plus a moment minimization constraint to the InSAR provides useful information: these data do not require slip over a large area near the trench at the southern end of the rupture.

The synthetic waveforms from the seismic only and joint inversions are shown in Figure 4.4. The fit to the seismic data is not significantly degraded by adding the InSAR data. Our tests indicate that including a fault plane with a variable dip is necessary to fit the seismic and geodetic data. These results are preliminary, as we plan future experiments with different weighting, including orbital ramps, and hypocenter shifts, as discussed above for the 1998 earthquake. Residual interferograms (subtracting predicted interferograms from the the InSAR only and joint models) are shown in Figure 4.8.

4.4.3 InSAR sensitivity to small, deep earthquakes

As a check on the sensitivity of the InSAR measurements and the catalog seismic locations, we have looked for the two largest earthquakes (besides the 1998 and 1995 earthquakes) to occur during the time when InSAR data are available. Both earthquakes are about M_w 6.6 and at 50 km depth, so the peak-to-peak LOS surface displacement is only 1.5-2 cm – of the same order as the atmospheric noise. The earthquake on 4/19/1996 is important to study, because it could contaminate estimates of post-seismic deformation (discussed below). Figure 4.9 includes a stack of several interferograms from this time period. Assuming that sources of noise in the interferograms (which are primarily due to atmospheric effects) are uncorrelated in independent interferograms, stacking the interferograms reduces the noise (Chapter 1). In this area, we find that the noise is usually correlated with topography (probably related to vertical stratification of the atmosphere, *Fujiwara et al.*, 1998; *Hanssen*, 2001), so the spatial pattern of the noise is very similar in independent interferograms, although the sign of the signal does reverse. We have selected interferograms to stack that seem to have the smallest atmospheric contamination, and with atmospheric contamination that is both positively and negatively correlated with topography.

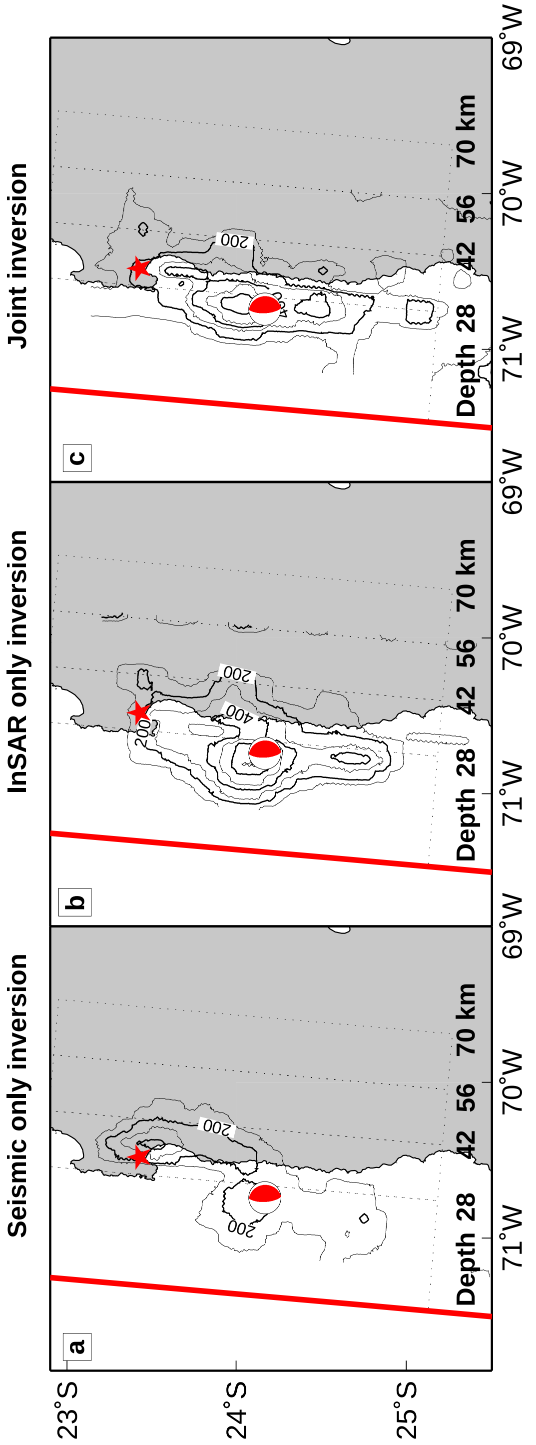

Figure 4.7: Contours of slip from the 1995 M_w 8.1 earthquake from inversions using only seismic data (a.), only InSAR data (b.), and both datasets (c.). The maximum slip is about 5 m and the contour interval is 1 m. The NEIC location is shown as the red star and the focal mechanism is from the Harvard catalog.

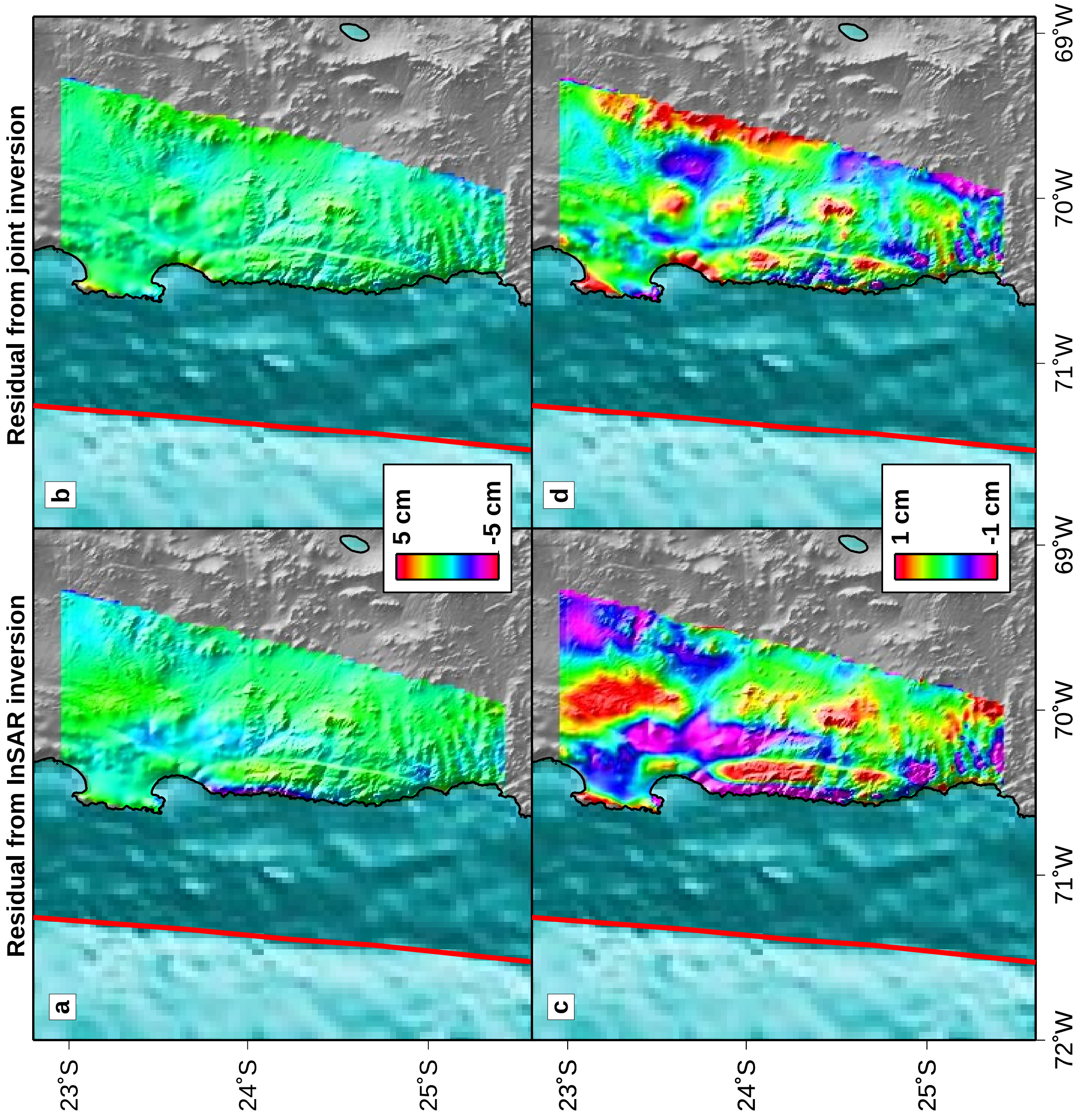

Figure 4.8: Residual of the InSAR data from track 96 for the 1995 M_w 8.1 from the inversions using only the InSAR data (a. and c. RMS 0.78 cm) and both seismic and InSAR data (b. and d. RMS 0.53 cm). The joint inversion only uses data from one satellite track (96), while the InSAR inversion uses data from all five tracks. Thus, the residual from the joint inversion is less than the InSAR only inversion. a. and b. The residual at the original wrap rate used in Figure 4.2, while c. and d. show the same residuals at an expanded color interval.

To determine the predicted LOS surface displacement from this earthquake, we have inverted seismic data and used the result to make a predicted interferogram. As with the other earthquakes, for the 4/19/1996 earthquake we used teleseismic displacements from azimuthally well distributed stations, using both P (15 stations) and SH waves (10 stations). We used the first 60 seconds for each wave type, and calculate the maximum slip to be about 0.5 m, giving an M_w 6.6. The maximum surface deformation signal from this earthquake is only about 1.5 cm in the LOS. In the stacked interferogram, there is a pattern with about the same magnitude and in about the same location (Figure 4.9). The noise in this interferogram is about the same amplitude as the signal, and the shape of the pattern is similar to local topography (the region of co-seismic uplift is in a topographic high, while the co-seismic subsidence is in a basin). However, we believe that the signal is real, because the pattern exists in several interferograms, where the atmospheric contamination is both positively and negatively correlated with topography. The maximum horizontal vector displacement at a GPS station from this earthquake is 0.6 cm, which is just barely above the noise level.

Figure 4.9 also shows an interferogram that spans a M_w 6.7 earthquake at a depth of about 50 km that occurred on 7/11/1993, and the prediction from our seismic waveform inversion (using 11 P and 6 SH records). Only one interferogram is available for this earthquake that does not include contamination from the 1995 earthquake, and so the observed signal is noisier. Yet there is a pattern of apparent ground uplift and subsidence in a location consistent with this earthquake. Both the 1993 and 1996 earthquakes appear to have nucleated close to their NEIC locations, and that the Harvard CMT locations are systematically shifted toward the trench.

4.4.4 Earthquakes from the 1980's

In order to compare the distribution of slip from the large earthquakes in the 90's with the earthquakes in the 1980's, we need reliable locations for the older events. Of particular interest are the large events: March 5, 1987, M_w 7.5; January, 19, 1988,

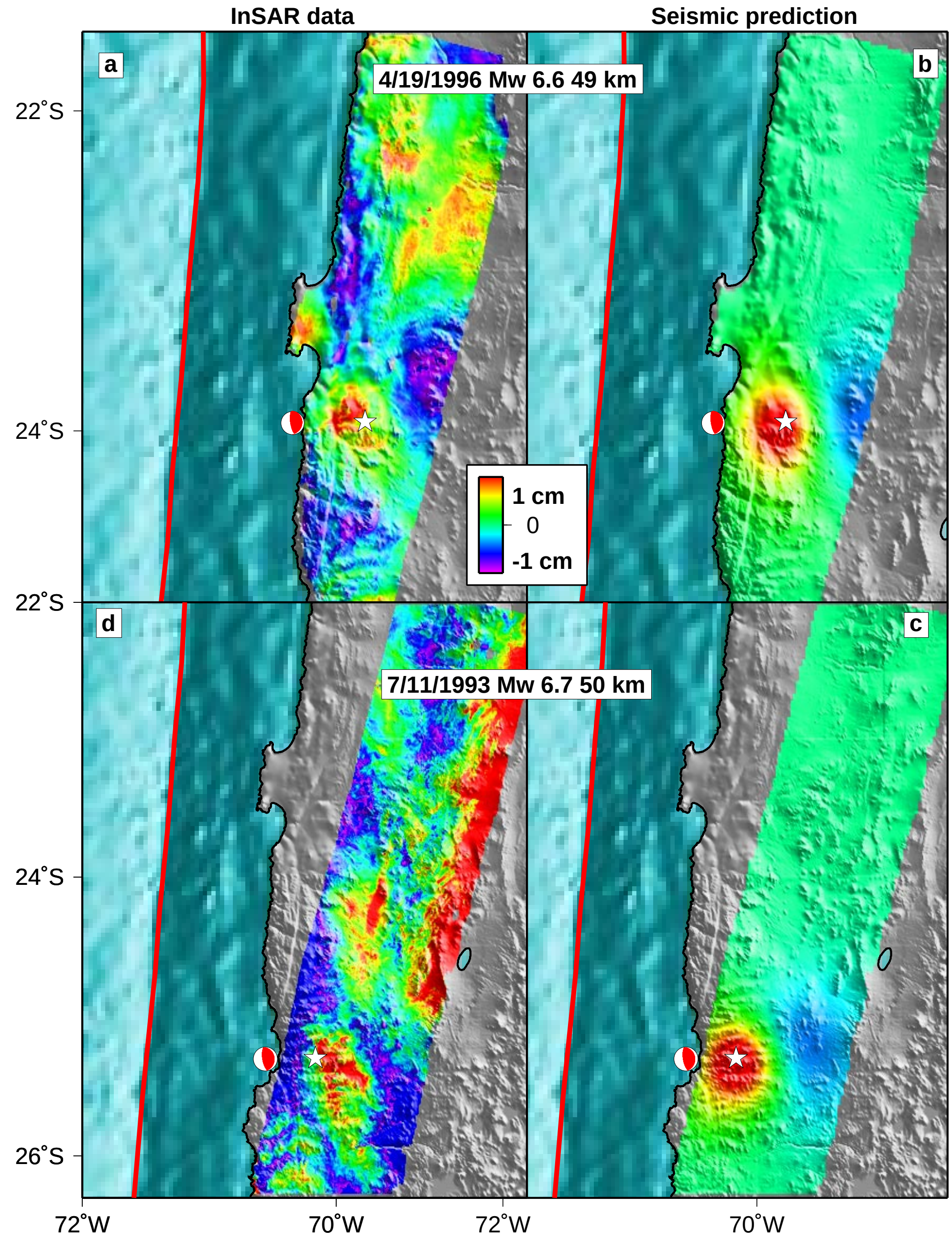

Figure 4.9: a. and c. LOS surface displacement that might be due to small deep earthquakes. b. and d. Predicted LOS displacements from seismic slip inversions. a. Stack of five interferograms: 4/21/1997-4/1/1996, 12/2/1996-3/31/1996, 11/17/1997-3/31/1996, 11/17/1997-4/1/1996, and 4/21/1997-3/31/1996. The largest earthquake during this collective timespan was M_w 6.6 on 4/19/1996 at about 50 km depth. The NEIC location is shown as a white star and the focal mechanism is from the Harvard catalog. b. The predicted LOS displacement from this earthquake from our seismic inversion (see text). c. We have only a single interferogram that spans the complete rupture area of the 7/11/1993 M_w 6.7 earthquake (also about 50 km depth) that does not include the effects of the 1995 M_w 8.1 event. This interferogram spans 7/11/1995-5/24/1992. d. The predicted surface LOS displacements from our seismic inversion for this event.

M_w 7.0; February 5, 1988, M_w 7.2 (all M_w from Harvard). The 1987 earthquake has been relocated using seismic waveforms (*Tichelaar and Ruff*, 1991; *Comte and Suárez*, 1995), and travel times have been used to relocate all the events (*Comte and Suárez*, 1995; *Engdahl et al.*, 1998). Although we expect these relocations to be accurate because they use depth phases (*Engdahl et al.*, 1998) or local stations (*Comte and Suárez*, 1995), we attempt to see if any improvement can be made through the use of InSAR data. We assume that the NEIC location is correct for the 1998 earthquake (the NEIC location had a lower RMS misfit in the joint inversion than the ISC or Engdahl *et al.* locations) and that the timing residuals for this earthquake can be considered station corrections (due to local or global velocity differences from the IASPEI91 model).

We apply these station corrections to travel time residuals calculated using the ISC P arrival picks and the predicted arrivals using the IASPEI91 velocity model. We do not use the time residuals straight from the ISC because they use the older Jeffrey-Bullen velocity model. We use the standard method of linearizing the travel time equation to relocate the events, and briefly summarize the technique (e.g., *Ruff et al.*, 1989). If the origin time or spatial location of an earthquake is wrong, there will be a systematic misfit of the P arrival time picks as a function of azimuth. The misfit has the form of a line: $dt + C * dy$; where dt is the error in origin time, dy is the horizontal distance to the correct location, and C is a constant related to the ray parameter and the angle between the station azimuth and the direction of hypocenter shift (θ), see Figure 4.10. For each angle θ, we do a two-iteration least-squares fit for dt and dy – we throw out data points that exceed 1.5 standard deviations in the first iteration. We also calculate the formal errors of the inversion (e.g., *Menke*, 1989). We only use stations at an epicentral distance between 30-99°, and don't include stations with a time residual greater than 3.5 seconds (e.g., *Engdahl et al.*, 1998), so that between 200-300 time picks are used in the inversions.

With the exception of the Harvard locations already mentioned, our earthquake relocations are similar to previous locations (Figure 4.11), considering the errors of our relocations (5-10 km), and the errors in previous relocations (10-15 km) (e.g., *Comte*

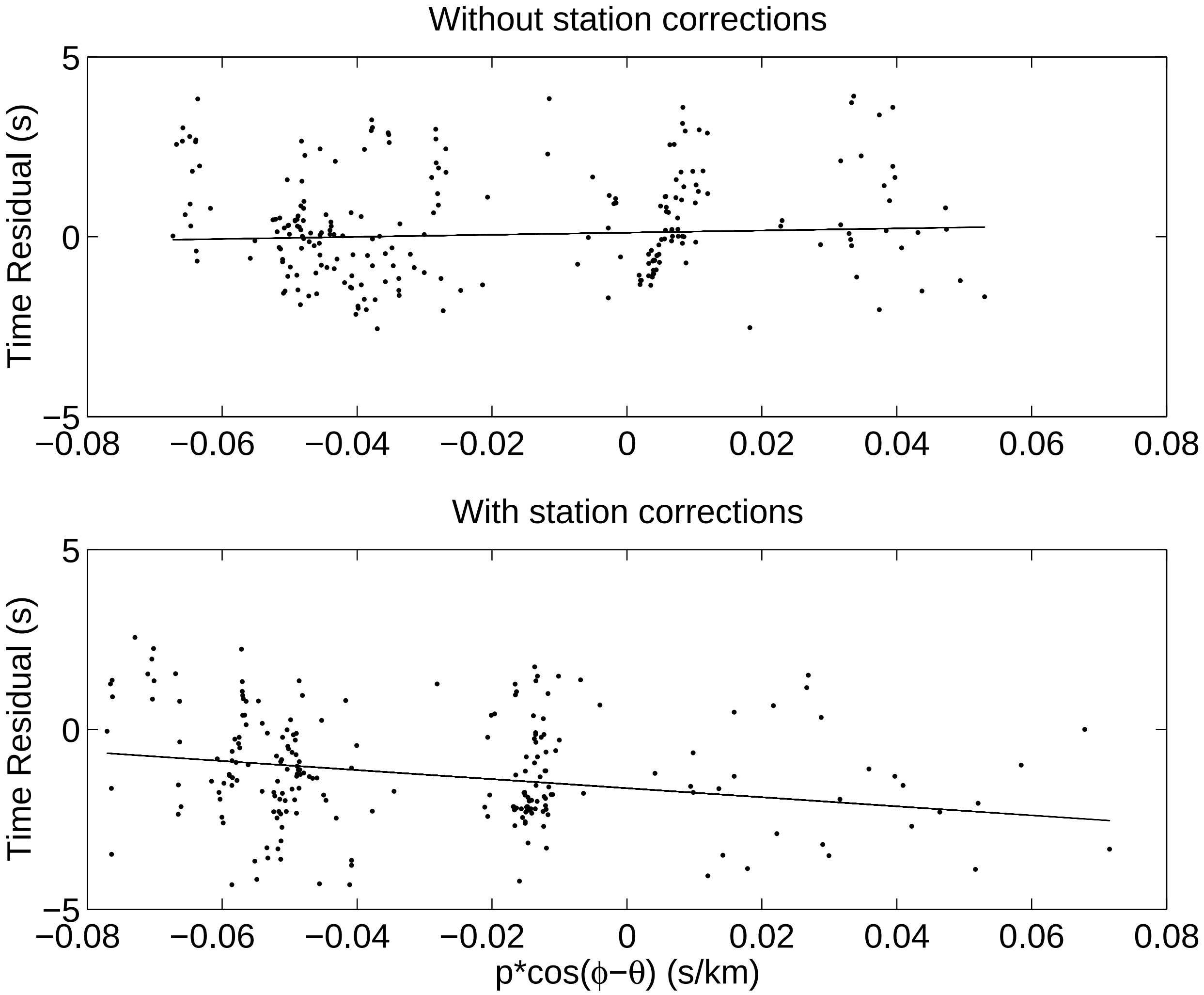

Figure 4.10: These plots show how we calculate the best fitting relocations for the 1987 earthquake. The points show the time residuals both with and without station corrections (plotted on the y axis) and the red line shows the best fitting line. The value of C from the text is plotted on the x axis, where p is the ray parameter, ϕ is the station azimuth, and θ is the direction of hypocenter shift (e.g., *Ruff et al.*, 1989). The RMS misfit is similar (1.5 seconds) for both inversions. The best fit parameters for the inversions done with and without station corrections are as follows: $\theta = 153°$ or 126°; dt = -1.6 ± 0.01 or 0.11 ± 0.01 s; dy = 12.6 ± 6 or 2.9 ± 5 km.

and Suárez, 1995). The similarity of our result to previous ones is expected because for most events the methodology is the same: using travel time picks. While we also try to use InSAR to determine station corrections, the addition of these corrections has little effect on the quality of the fit or the earthquake relocation (Figure 4.10). It is surprising that the addition of station corrections does not improve the fit, and we suspect that one or more of our assumptions might be incorrect. Perhaps the 1998 NEIC location is not really the exact location, or perhaps the travel time residuals for this event are not due to earth structure but are due to random noise at the stations. We also implicitly assume that the station corrections are the same in 1998 and in the 1980's, and this might not be the case if the station was moved. More precise relocations might be possible by correlating the seismic waveforms (e.g., *Waldhauser and Ellsworth*, 2000).

We have not yet attempted detailed slip inversions for two reasons: (1) the small magnitudes of these events means that the rupture size is limited compared to the large fault plane in northern Chile (the earthquakes are nearly point sources like the 1998 event); (2) very few digital waveforms are publically available. To constrain the size of the rupture and the magnitude of slip, we can use the rupture duration calculated from waveform inversions for the 1987 earthquake – between 12-17 seconds (*Comte and Suárez*, 1995; *Tichelaar and Ruff*, 1991), and we use the average 15 seconds. We assume the rupture is ellipsoidal with a ratio of length/width = 2, and that the rupture velocity is 3 km/s (similar to the 1995 and 1998 earthquakes). The rupture duration has not been calculated for the 1988 earthquakes, so we assume a duration of 10 seconds from comparison with earthquakes of similar size (the 1998 earthquake, *Comte and Suárez*, 1995; *Tichelaar and Ruff*, 1991). Using the calculated area of rupture (A) and the seismic moment M_o, we calculate the magnitude of slip using the standard relation $D = \frac{M_o}{\mu A}$, where $\mu = 3.2 \times 10^{10}$ Pa is the rigidity. The seismic moments (all from Harvard) and average slip are as follows: 2.5×10^{20} Nm and 1.5 m for 1987; 3.5×10^{19} Nm and 0.4 m for January 1988; and 6.6×10^{19} Nm and 0.7 m for February 1988.

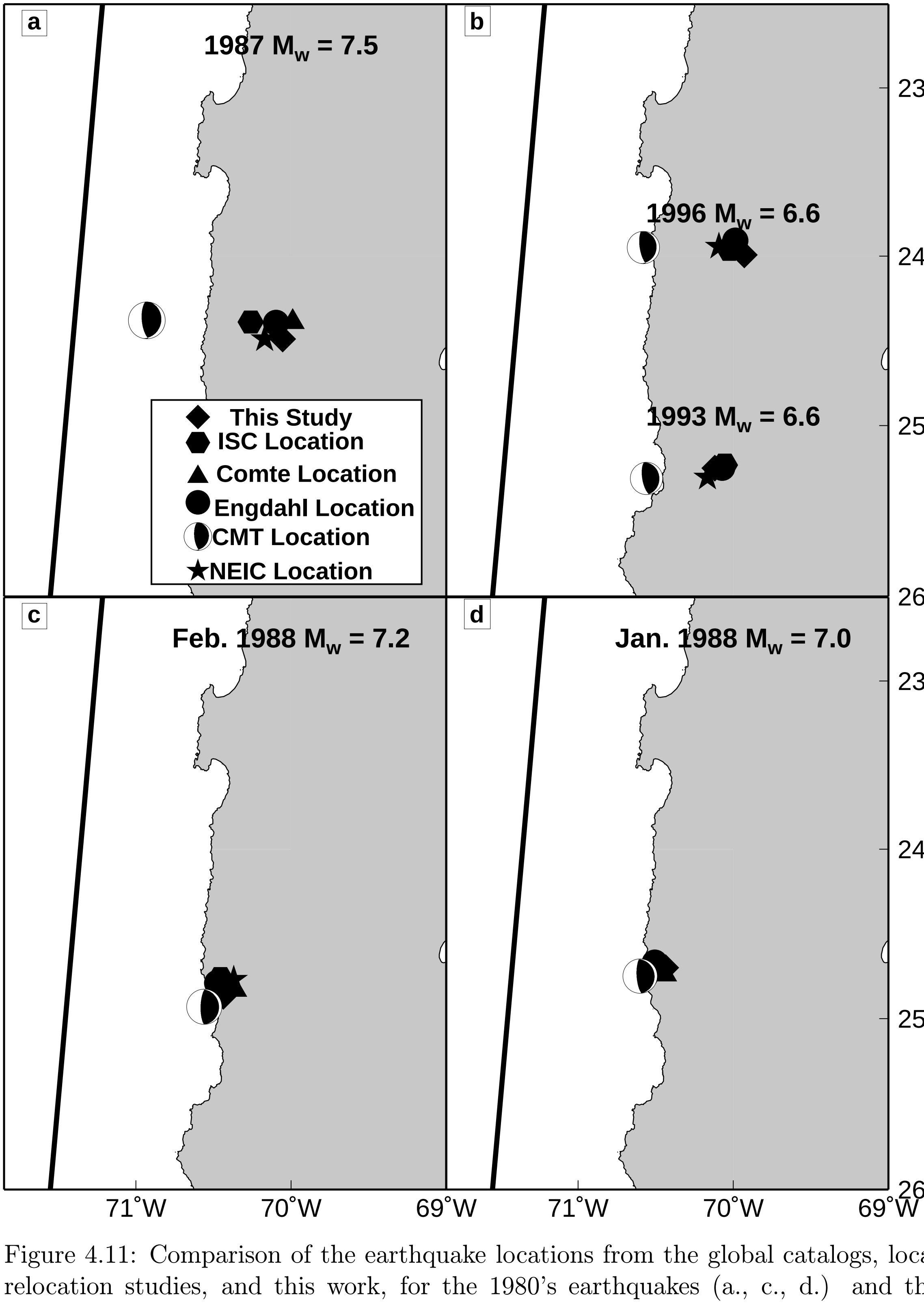

Figure 4.11: Comparison of the earthquake locations from the global catalogs, local relocation studies, and this work, for the 1980's earthquakes (a., c., d.) and the small, deep events in the 1990's (b.). The Harvard CMT locations are systematically mislocated towards the trench for the 1987, 1993 and 1996 earthquakes, but all other locations are clustered within 10-15 km of each other (roughly within the error bounds of the relocations).

4.4.5 Post-seismic 1995-1996

Within the past decade, measurements of deformation immediately following several subduction zone earthquakes reveal that a large amount of slip has occurred aseismically during a few weeks to months (e.g., *Melbourne et al.*, 2002, Table 1). This post-seismic deformation occurs over a much shorter period than would be expected for visco-elastic relaxation of the bulk material (years-decades), and visco-elastic relaxation models provide a poor fit to the data in at least one location (*Azúa et al.*, 2002). Therefore, the deformation is thought to be caused by another process – afterslip on the fault interface or across a fault zone.

Afterslip is predicted to occur in regions where there was little co-seismic slip and where the frictional properties of the fault zone are such that delayed, slow slip is triggered by the earthquake (e.g., *Scholz*, 1998; *Marone*, 1998). The existence of afterslip implies that a large fraction of the strain accumulated by plate convergence is not released in earthquakes. Determining the location and magnitude of afterslip is important for understanding the strain budget of subduction zones (e.g., *Pacheco et al.*, 1993). We use InSAR and GPS measurements to place constraints on the location and amplitude of afterslip during the time period when both observations are available – the first 15 months after the 1995 earthquake. We expect the majority of any afterslip to be during this time interval, because afterslip is often characterized by an initially high rate of deformation followed by a logarithmic decay (e.g., *Marone et al.*, 1991; *Melbourne et al.*, 2002).

Alternatively, the deformation could be due to pore pressure changes in the bulk crustal materials caused by post-seismic fluid flow induced by co-seismic stress changes (e.g., *Peltzer et al.*, 1996; *Jónsson*, 2002). There is seismic evidence for yet another fluid flow mechanism involving the migration of fluids from the subducting plate across the fault interface following the 1995 earthquake (*Husen and Kissling*, 2001), but calculations of the deformation signal from this process will be the subject of future work. Over the short co-seismic time interval, there is no time for fluids to readjust to stress variations, and so the material behaves as if its elastic moduli (*i.e.*, Poisson's ratio, ν) are undrained (e.g., *Wang*, 2000). During the post-seismic time interval, the pore pressure variations are reduced, and the elastic moduli will relax to their drained values. To get a sense of the potential magnitude and shape of the deformation signal associated with this pore fluid flow, we can subtract the co-seismic deformation field calculated using the undrained moduli from the drained deformation field (*Peltzer et al.*, 1998; *Jónsson*, 2002). The values of ν for appropriate materials and pressures are poorly constrained (e.g., *Roeloffs*, 1996), but values of 0.25 and 0.29 for the drained and undrained ν are plausible (*Rice and Cleary*, 1976; *Wang*, 2000). In Figure 4.12, we have used these values of ν, along with our co-seismic slip map for the 1995 earthquake from Chapter 3 to predict the direction and amplitude (to an order of magnitude) of the deformation from the fluid flow. We assume a single value of ν for the entire crust and that the drained condition is quickly achieved (in less than 1 year). A more realistic calculation must account for the spatial variations in the elastic moduli (instead of the average values used here), especially variations with depth, and more accurately assess the time evolution (e.g., *Masterlark et al.*, 2001). Nonetheless, the GPS displacements from this mechanism are opposite those observed (Figure 4.12), so we conclude that bulk crustal fluid flow is not solely responsible for the deformation and that another mechanism (assumed to be afterslip) must have occurred.

We use GPS displacements from the SAGA array spanning the time period from October-November 1995 to October-November 1996 (3-15 months post-seismic, Figure 4.13) (*Klotz et al.*, 2001) and several interferograms (Figure 4.14). The campaign GPS measurements do not begin until several months after the earthquake. Data from the continuous GPS station in the city of Antofagasta spanning the first month post-seismic exists (*Melbourne et al.*, 2002), and a SAR scene from track 96 was acquired 9.5 hours after the earthquake, meaning that the interferograms in Figure 4.14 record any deformation after that time. At present, only the horizontal GPS displacements have been published, although work is continuing on the vertical component which is, of course, noisier (J. Klotz, personal communication, 2002). Because the InSAR is mostly sensitive to vertical deformation, the two datasets are complimentary.

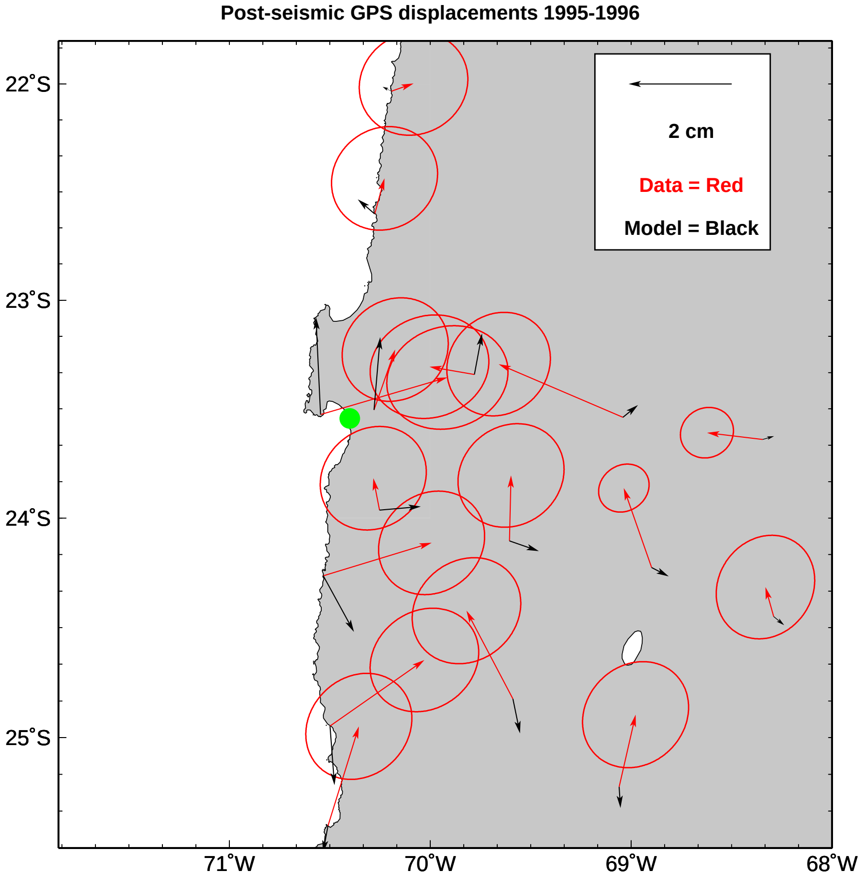

Figure 4.12: The black arrows show the predicted horizontal deformation from bulk fluid flow, assuming that co-seismic deformation occurred at an undrained $\nu = 0.29$ and that the measurements are taken after the crust returns to a drained condition ($\nu = 0.25$). Changing the values of ν will effect the magnitude of the deformation, but not the general pattern. GPS data are shown as the red arrows (*Klotz et al.*, 2001).

Post-seismic GPS data has also been collected from the ten-station French-Chilean array in the Antofagasta area (*Ruegg et al.*, 1996) and is being analyzed by M. Chlieh (manuscript in preparation, 2003).

The horizontal displacements of GPS stations from several arrays are shown in Figure 4.15. During the 1990's the majority of the stations in South America between 10°-45°S move in about the same direction as the subducting Nazca plate, as would be expected during the inter-seismic time interval when the plates are locked together (*Savage*, 1983). However, the displacement of stations within the rupture areas of the 1960 and 1995 Chile earthquakes was different from that predicted by the inter-seismic model, and is likely due to post-seismic deformation (*Klotz et al.*, 2001). In the Antofagasta region, the stations near the coast move in the direction predicted for the inter-seismic period, but those further inland do not (Figure 4.13). We assume that this deformation is caused by afterslip, based on the arguments given above, so that in the modeling below, we approximate both afterslip and inter-seismic locking of the fault as dislocations on the fault interface (*Savage*, 1983).

It is difficult to constrain the temporal evolution of the afterslip. There is no obvious deformation during the first month post-seismic at the continuous GPS station in Antofagasta (*Melbourne et al.*, 2002) (Figure 4.13). Further data from this station might provide constraints on the timing of deformation, but unfortunately, the station location is not optimal for measuring the afterslip and could be overwhelmed by the signature of inter-seismic deformation. The InSAR data does provide more temporal coverage than the GPS data, but it is difficult to determine whether there is a clear signature of post-seismic deformation in the InSAR data (Figure 4.14). The phase variations in the images are correlated with topography, and so we think that the signal is due to vertical stratification of the atmosphere. A correlation between InSAR phase and topography is seen in many locations (e.g., *Fujiwara et al.*, 1998, Chapter 2), and challenges the common assumption that atmospheric noise is spatially random. Because the correlation between phase and topography is both positive and negative it is useful to stack images together so that this effect partly cancels. However, in this area, there are more scenes with the positive than negative correla-

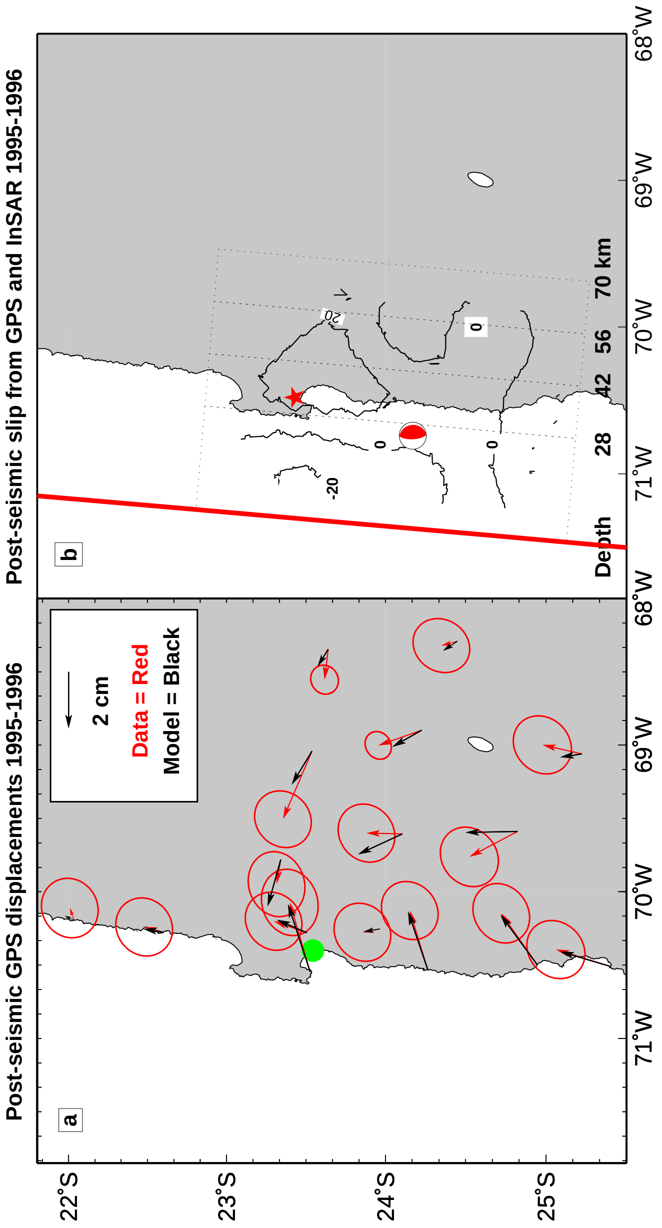

Figure 4.13: a. Red lines show the horizontal GPS post-seismic deformation following the 1995 M_w 8.1 earthquake between 1996-1995, including the error ellipses (*Klotz et al.*, 2001). The black lines show the modeled displacements from our joint InSAR and GPS inversion for slip (shown in b.). The green circle shows the location of the continuous GPS station in Antofagasta. b. Contours of post-seismic slip between 1996-1995 from a joint InSAR and GPS inversion. The maximum slip amplitude is 0.25 m and the contour interval is 0.2 m. The star and mechanism shows the NEIC and CMT locations for the 1995 M_w 8.1 earthquake.

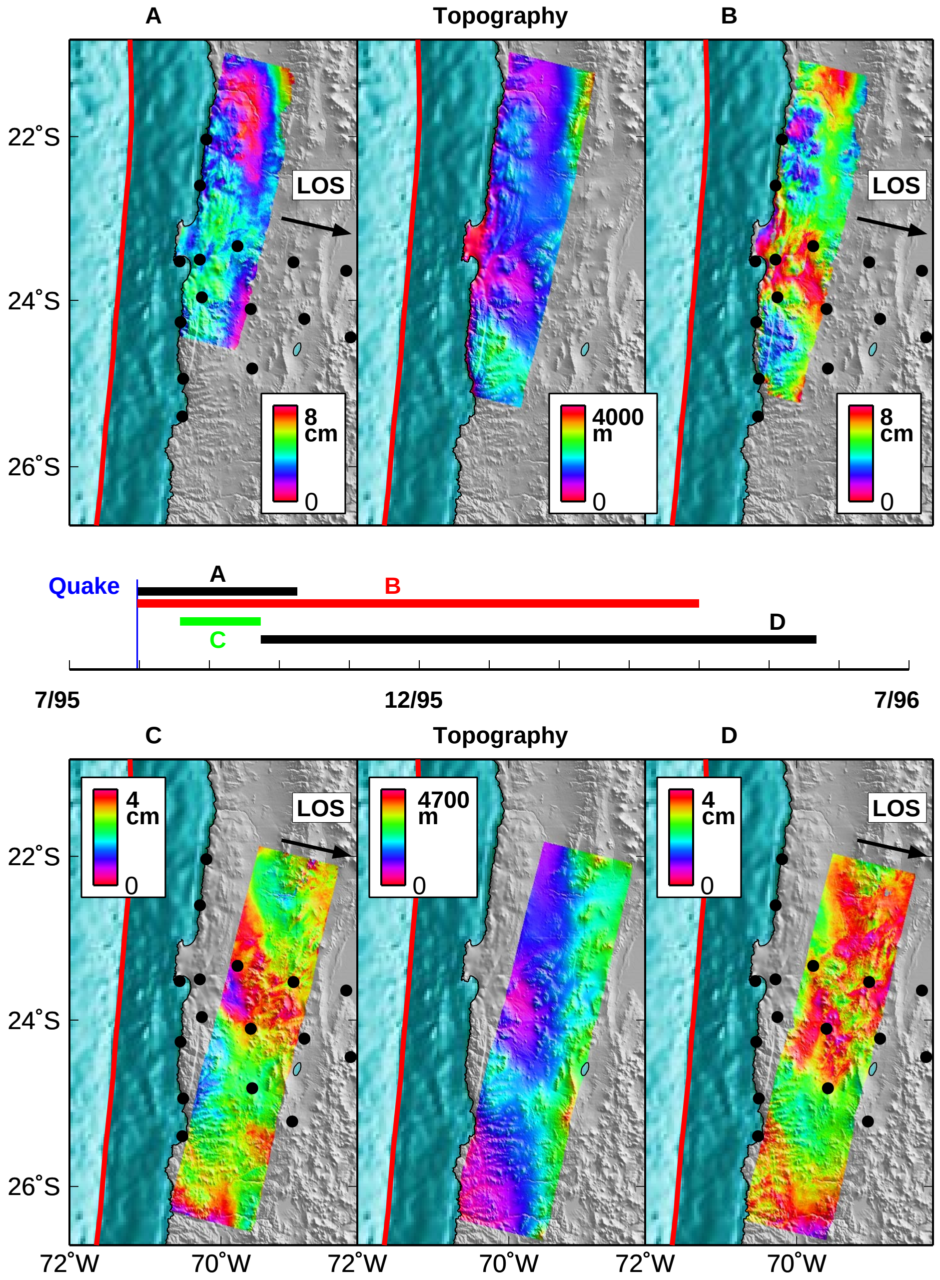

Figure 4.14: InSAR observations during the first year post-seismic from four interferograms from tracks 96 (A and B) and 325 (C and D) spanning roughly the same time period as the GPS observations (Figure 4.13). For comparison with the interferograms, the topography along each track of data is shown in center position of the top and bottom rows. The time periods of the interferograms compared to the time of the 1995 M_w 8.1 earthquake are shown in the center of the plot and are as follows: A. 10/8/1995-7/30/1995 B. 3/31/1996-7/30/1995 C. 9/19/1995-8/15/1995 D. 5/21/1996-9/19/1995. The black circles are the GPS points shown in Figure 4.13 (*Klotz et al.*, 2001).

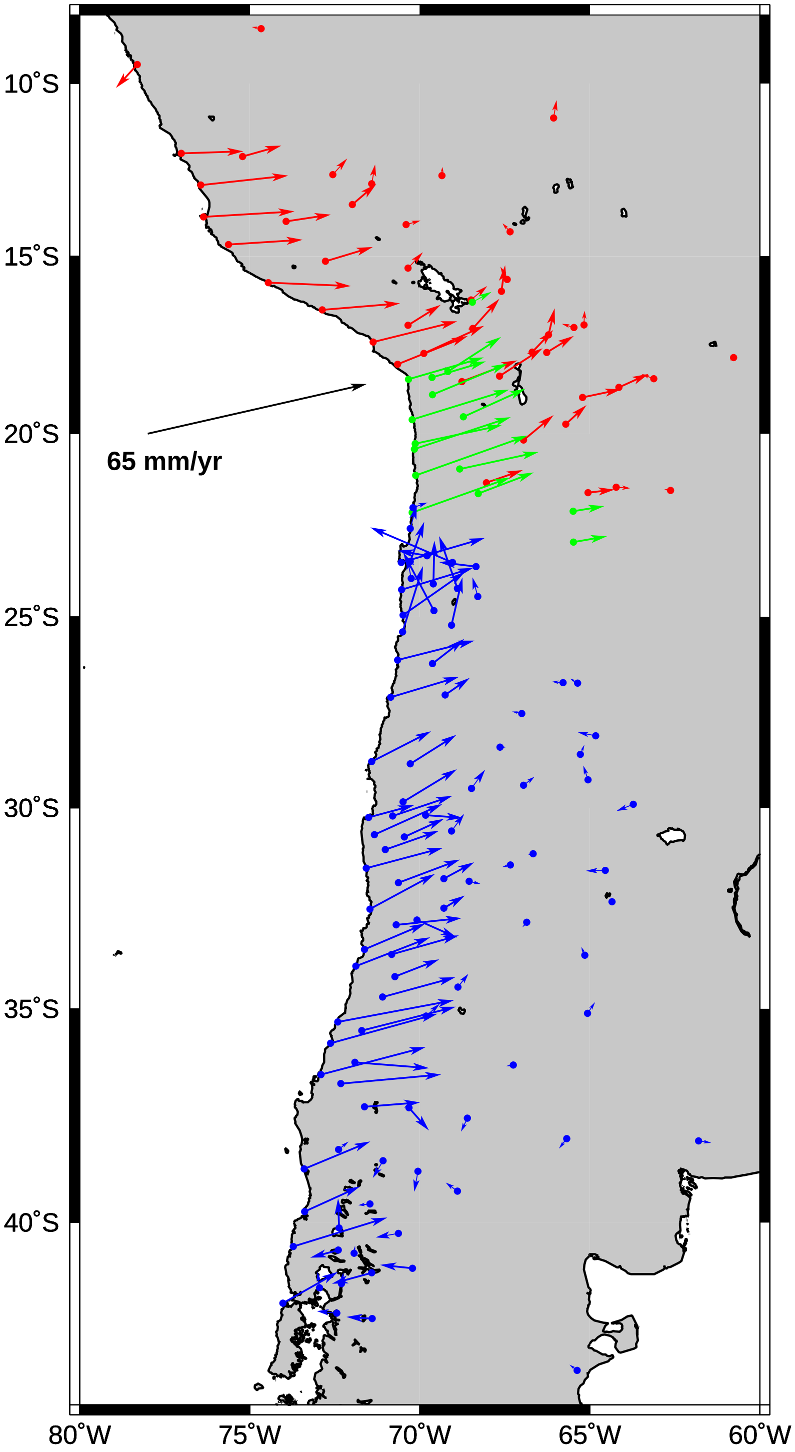

Figure 4.15: Published displacements of GPS stations in South America – more measurements exist (e.g., *Ruegg et al.*, 1996), but are not publically available. The colors correspond to different arrays – red is from SNAPP (*Norabuena et al.*, 1998), but the velocities are from (*Bevis et al.*, 1999; *Kendrick et al.*, 2001) so that a common reference frame is used; green is from CAP (*Kendrick et al.*, 1999); blue is from SAGA (*Klotz et al.*, 2001). The error ellipses have been removed for the clarity of presentation. The relative Nazca-South American convergence rate and direction is shown by the black arrow (*Angermann et al.*, 1999).

tion. The existence of these persistent atmospheric effects in such an arid region as the Atacama desert compels us to caution those who are looking for a deformation signal that is correlated with topography in other areas, even if they are stacking interferograms.

We attempt to correct for the tropospheric contamination by determining the linear function that best relates the phase signal to the topography over the entire image, and then removing it (see Chapter 2). However, we found that this correction had little effect, because the horizontal variations in the linear function were of equal or more importance than the vertical variations. The large horizontal variations are expected because of the lateral difference in water vapor content (related to, for example, distance to the coast). The lack of clear deformation in the InSAR is not inconsistent with the GPS result, because the signal-to-noise ratio of a single interferogram is lower than the horizontal GPS measurements. The InSAR data is still useful in providing constraints as to where slip did not occur. There are several large gaps in the GPS coverage, and inversions for slip that only include GPS data predict sizable vertical deformation in those data gaps that is not consistent with the InSAR results. Therefore, our inversions are more accurate when we use both datasets.

We invert the GPS and InSAR observations (Figures 4.13 and 4.14) for slip on the fault interface (as defined in Chapter 3) in an elastic half-space. We use a linear inversion with smoothing, where the weighting of the smoothing parameter was chosen empirically to give a smooth solution that also fits the data (see Chapter 5). We do not constrain the sign of the slip because some parts of the fault interface appear locked (based on the eastward motion of the GPS coastal stations), and a locked fault can be simulated by a normal dislocation (*Savage*, 1983). While the shallow parts of the fault appear at least partially locked, we infer that other portions, particularly under the Mejillones Peninsula, are undergoing afterslip (Figure 4.13). The maximum amplitude of the after-slip is about 25 cm, and if we only count the patches that are slipping in a reverse sense, the moment is about 1.5×10^{19} Nm), which is only about 5-10% of the co-seismic moment release.

4.4.6 Post-seismic 1995-2000

We use InSAR to constrain the post-seismic deformation beyond the first 15 months following the earthquake. GPS data is presently only available for 1995-1996, but preliminary analysis of data from 1997, indicates a much smaller amplitude displacement than during the previous year (*Klotz et al.*, 2000). We have made 25 interferograms (spanning 4-6 frames) that do not include either the 1995 or 1998 earthquakes (Table 4.1), including one interferogram before the 1995 event (track 325: 7/11/1995-5/24/1992, Figure 4.9), many interferograms spanning the time interval between the events (track 96: 7/30/1995-11/17/1997) and one interferogram after the 1998 event (track 96: 12/7/1998-3/6/2000, Figure 4.16).

We have stacked 11 interferograms together spanning the time between the 1995 and 1998 earthquakes (7/30/1995-11/17/1997, Figure 4.16), and removed the effects of the 1996 earthquake. Before stacking, we estimated the quadratic orbital baseline parameters that minimized the phase signal in each interferogram, in order to remove possible long-wavelength signals from inter-seismic coupling and errors in the orbits (see Chapter 3). While necessary to remove orbital errors, this process can also remove real tectonic deformation that occurs at a long wavelength. At present, the only way to reliably measure such long wavelength deformation is with GPS or other ground-based observations. If the GPS stations are sufficiently dense spatially and the timespan of observations is similar to the InSAR data, the GPS displacements can be used in the re-estimation of the orbital parameters. Thus, by using both datasets, the InSAR data becomes sensitive to the long-wavelength deformation. However, we are currently unable to combine the InSAR and GPS within our study area in this way because of the short timespan of the GPS observations, their limited spatial extent, and the lack of calculated vertical displacements.

The stacked image is sensitive to short-wavelength deformation, and it is remarkable that there is less than 2 cm peak-to-peak displacement in 2.3 years. The largest deformation signal occurs north of the primary rupture area of the 1995 earthquake – on the Mejillones Peninsula and north-ward. Uplift at the Mejillones Peninsula

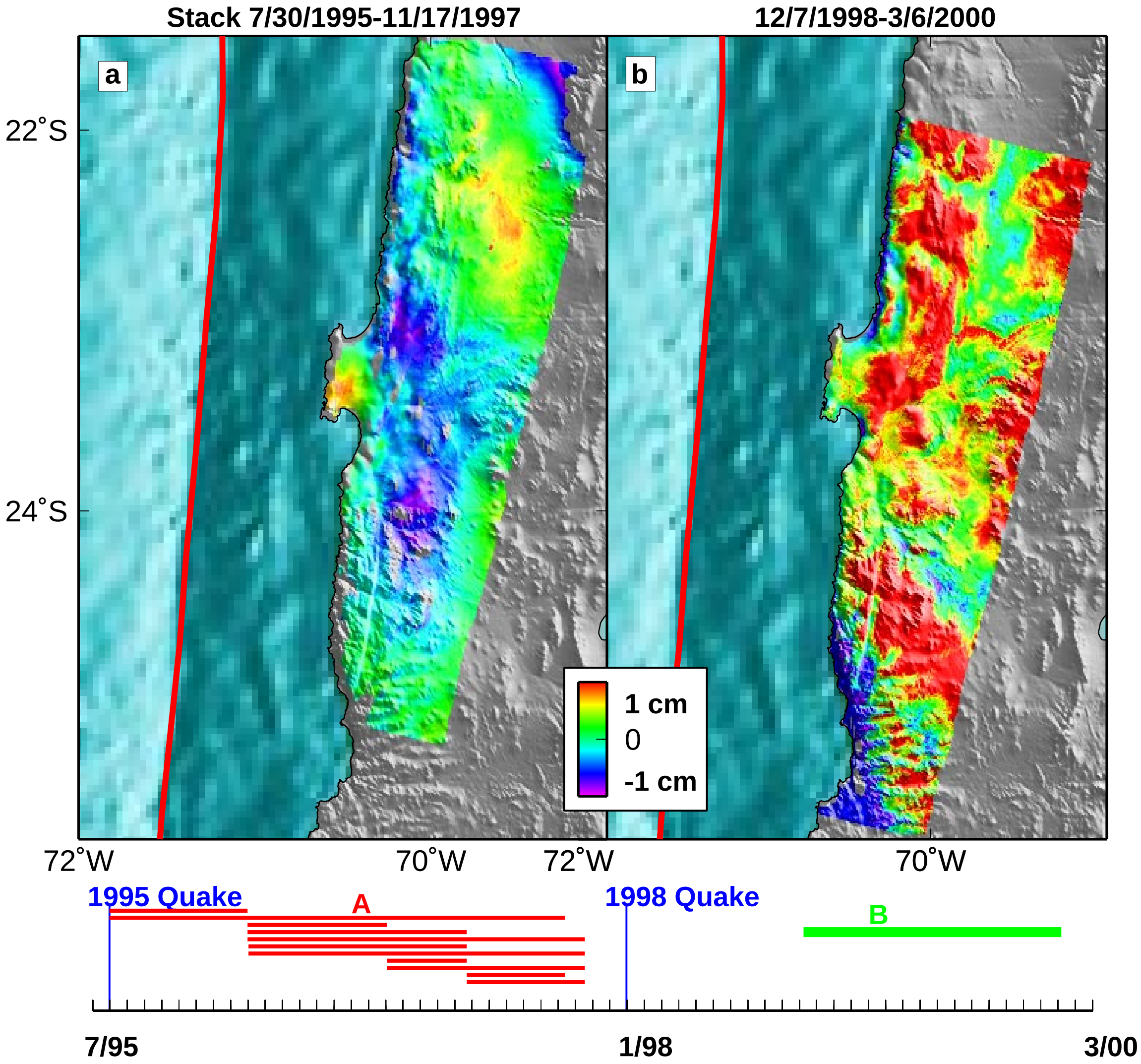

Figure 4.16: a. Stack of 11 interferograms spanning 7/30/1995-11/17/1997 (see Table 4.1 for specific interferograms) with our model of the 1996 M_w 6.6 earthquake removed (Figure 4.9). b. The longest-time period interferogram spanning the post-seismic time interval after the 1998 earthquake that we can make.

and adjacent subsidence is consistent with afterslip shown in Figure 4.13, and uplift further north (within the rupture area of the 1877 earthquake) is consistent with inter-seismic loading. In fact, the GPS stations in this area (PCUA and TOPI) did not move between 1995-1996, perhaps hinting at anomalous behavior in this area. The presence of post-seismic deformation in this area will be tested once the vertical GPS displacements are calculated, the data from the continuous station in Antofagasta is available, and the GPS data from 1997 is published. There is no clear tectonic deformation (only phase correlated with topography) in the interferogram we have made following the 1998 earthquake (Figure 4.16).

We have used nearly all of the possible post-seismic InSAR data. Attempts to create interferograms spanning into 2002 were unsuccessful because the new ERS-2 acquisitions appear to be on the incorrect Doppler ambiguity, although the ESA website indicated otherwise (http://earth.esa.int/pcs/ers/sar/doppler/doppler_query/). Although our dataset covering the post-seismic time interval is not complete (we have about 50% of all data acquired for track 96, all of tracks 361 and 89, 60% of track 325, and about 40% of track 368), additional acquisitions of archived data before 2000 would add little to resolving the temporal evolution of the post-seismic deformation. The remaining data either have unfavorable baselines or scenes missing from the area of interest.

4.5 Discussion

There is only limited overlap between the five recent $M_w > 7$ earthquakes in northern Chile (Figure 4.17). Each earthquake appears to rupture a different part of the fault plane, although the magnitude of slip in each area is different (5 m in the 1995 event, and < 1 m in areas around the $M_w \sim 7$ earthquakes). The slip deficit near the small events must be released in other earthquakes or in aseismic slip. We find little aseismic slip in the 1990's, although geologic observations require some post-seismic slip to cancel co-seismic subsidence over the long term (*Delouis et al.*, 1998). Based on our sensitivity to the M_w 6.6 events in 1993 and 1996, we think that if there were silent slip events between 1992-2000 like those in Cascadia (M_w 6.7, 30-50 km deep, every 14 months, *Miller et al.*, 2002), we would have detected them.

It is interesting to note that the 1995 earthquake did not rupture to the bottom of the seismogenic zone (between 40-50 km, based on the maximum depth of thrust events on the fault interface, *Tichelaar and Ruff*, 1991; *Suarez and Comte*, 1993; *Tichelaar and Ruff*, 1993a; *Comte et al.*, 1994; *Delouis et al.*, 1996; *Husen et al.*, 1999), and that the bottom 10 km of depth ruptured in the $M_w \sim 7$ events in 1998 and 1987. Perhaps variations in material properties as a function of depth do not allow large events to reach the bottom of the seismogenic region, and only small events can occur in that region. In fact, the eastern limit of rupture in the 1995 event seems to be roughly similar to the Chilean coastline, as has been observed elsewhere (*Ruff and Tichelaar*, 1996). The location of the coastline is roughly related to where the Moho intersects the subducting plate (*Ruff and Tichelaar*, 1996), and so this material interface might effect the downdip seismic limit (*Tichelaar and Ruff*, 1991). In northern Chile, near the coast, the Moho is between 40-50 km (*Wigger et al.*, 1994), but the exact location of the intersection of the Moho with the subducting plate is not known. In other subduction zones (*e.g.,* Cascadia and Nankai), temperature seems to control the downdip limit (350-450°C), but the northern Chile subduction zone is so cold that these temperatures are not reached until 70 km because of the old age of the Nazca plate, and the lack of insulating sediments (*Oleskevich et al.*, 1999).

We can not explain why there is a consistent mislocation of the Harvard CMT's of $M_w < 8$ earthquakes toward trench, although we suspect the 3-D velocity variations are important. From our joint InSAR and seismic inversions and relocations of events, it it seems that other global catalogs provide more accurate locations in this area.

In several subduction zones, the equivalent moment of the post-seismic deformation is equal to or exceeds the co-seismic moment release (Table 4.2). This rapid post-seismic deformation might actually be common among historic earthquakes, but missed because of the lack of continuous recordings of deformation. The little post-seismic deformation following the 1995 Antofagasta earthquake appears anomalous, particularly considering that the nearby 2001 M_w 8.4 Arequipa, Peru, earthquake

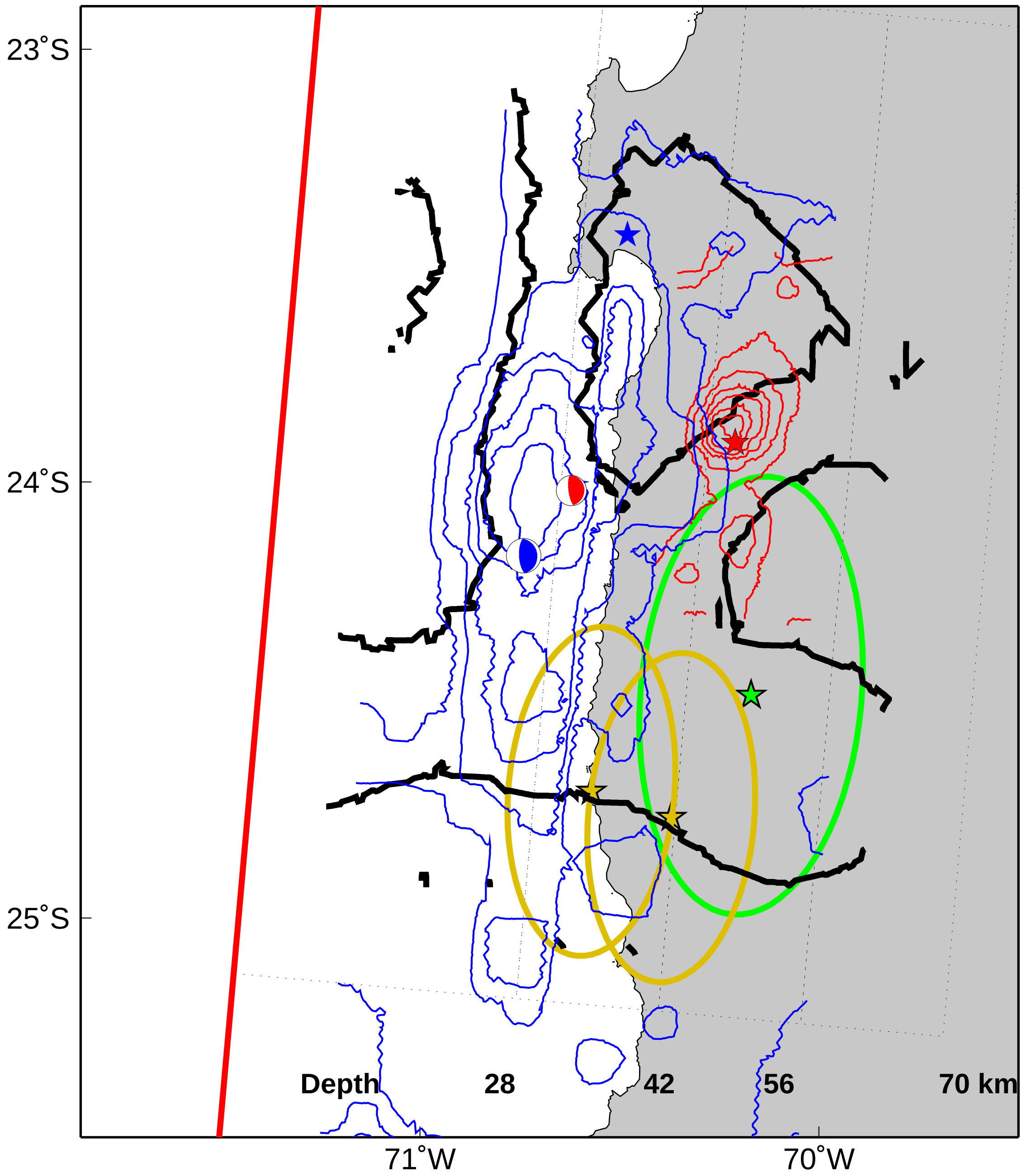

Figure 4.17: The location of slip on the fault interface in the northern Chile subduction zone from aseismic slip and earthquakes with $M_w > 7$ since 1987 as determined in this chapter. Symbols are the same as in Figure 4.9, and the colors are associated with the different events: blue is the 1995 earthquake, red is the 1998 earthquake, black is associated with post-seismic deformation, green is the 1987 earthquake (average slip 1.5 m), and brown are the 1998 earthquakes (mean 0.4 m slip for January and 0.7 m for February).

has much more significant post-seismic deformation. In Chapter 5, we compare the characteristics of these earthquakes and their subduction zones, and offer possible explanations for the difference in afterslip.

Earthquake	Co-seismic Moment	Post-seismic (fraction of co-seismic moment)	Method	α[11]
2001 Arequipa, Peru[1,2]	8.4	20% in 4 months	GPS	0.16-0.86[12]
1997 Kronotsky, Kamchatka[3]	7.8	100% in 1-3 months	GPS	0.49-1[13]
1996 Nazca, Peru[4]	7.7	$<$ 10% after first 60 days	InSAR	0.16-0.86[12]
1996 Hyuga-nada, Japan[5]	2 quakes each 6.7	100% in $\sim$ 1 year	GPS	NA[14]
1995 Jalisco, Mexico[2,6]	8.0	47% in 5 months	GPS	0.26-0.64[13]
1995 Antofagasta, Chile[2,7]	8.1	5% in 15 months	InSAR/GPS	0.01-0.84[12]
1994 Sanriku-Oki, Japan[2,8]	7.7	$>$ 100% in 1 year	GPS	0.18-0.25[13]
1992 Sanriku-Oki[9]	6.9	100% in 5 days	strainmeter	0.18-0.33[13]
1989 Sanriku-Oki[10]	7.4	100% in 50 days	strainmeter	0.18-0.33[13]

Table 4.2: Comparision of the magnitude of post-seismic slip immediately following subduction zone earthquakes from around the world. The timescale for the deformation sometimes refers to the time for there to be no more "appreciable slip" (as defined by the authors), while in other instances it refers to the decay time (time for deformation to become $1/e$ of the initial value). We have attempted to better compare the timescales by multiplying the decay time by 5, which is the time needed to account for 99.99% of the slip. Data sources for table: [1]*Ruegg et al.* (2001); [2]*Melbourne et al.* (2002); [3]*Bürgmann et al.* (2001); *Gordeev et al.* (2001); [4] Chapter 5; [5]*Hirose et al.* (1999); *Yagi et al.* (2001); *Ozawa et al.* (2001); *Miyazaki et al.* (2003); [6]*Hutton et al.* (2002); [7]this study; [8]*Heki et al.* (1997); *Heki and Tamura* (1997); *Nishimura et al.* (2000); [9]*Kawasaki et al.* (1995); [10]*Kawasaki et al.* (2001); [11]Seismic coupling coefficient (see Chapter 5); [12]*Peterson and Seno* (1984); *Scholz and Campos* (1995); [13]*Pacheco et al.* (1993); [14]Not Available – this region is transitional between the highly coupled Nankai Trough and weakly coupled Ryuku arc (*Ito et al.*, 1999).